





# Variations in Wave Slope and Momentum Flux From Wave-Current Interactions in the Tropical Trade Winds

Suneil Iyer<sup>1,2</sup> , Jim Thomson<sup>1</sup> , Elizabeth Thompson<sup>3</sup> , and Kyla Drushka<sup>1,2</sup> 

<sup>1</sup>Applied Physics Laboratory, University of Washington, Seattle, WA, USA, <sup>2</sup>School of Oceanography, University of Washington, Seattle, WA, USA, <sup>3</sup>NOAA Physical Sciences Laboratory, Boulder, CO, USA

## Key Points:

- Six Lagrangian surface drifters observed wave spectra in an area of moderate mesoscale activity in the northwestern tropical Atlantic
- Surface current and wind-wave directions were opposed over 30% of the time; during this time wave mean square slope was elevated
- Wave-current interactions caused variations in air-sea momentum flux of at least 6% at wind speeds over 8 ms<sup>-1</sup>

## Correspondence to:

S. Iyer,  
[iyersk@uw.edu](mailto:iyersk@uw.edu)

## Citation:

Iyer, S., Thomson, J., Thompson, E., & Drushka, K. (2022). Variations in wave slope and momentum flux from wave-current interactions in the tropical trade winds. *Journal of Geophysical Research: Oceans*, 127, e2021JC018003. <https://doi.org/10.1029/2021JC018003>

Received 14 SEP 2021  
Accepted 3 MAR 2022

**Abstract** Observations from six Lagrangian Surface Wave Instrument Float with Tracking drifters in January-February 2020 in the northwestern tropical Atlantic during the Atlantic Tradewind Ocean-atmosphere Mesoscale Interaction Campaign are used to evaluate the influence of wave-current interactions on wave slope and momentum flux. At observed wind speeds of 4–12 ms<sup>-1</sup>, wave mean square slopes are positively correlated with wind speed. Wave-relative surface currents varied significantly, from opposing the wave direction at 0.24 ms<sup>-1</sup> to following the waves at 0.47 ms<sup>-1</sup>. Wave slopes are 5%–10% higher when surface currents oppose the waves compared to when currents strongly follow the waves, consistent with a conservation of wave energy flux across gradients in currents. Assuming an equilibrium frequency range in the wave spectrum, wave slope is proportional to wind friction velocity and momentum flux. The observed variation in wave slope equates to a 10%–20% variation in momentum flux over the range of observed wind speeds (4–12 ms<sup>-1</sup>), with larger variations at higher winds. At wind speeds over 8 ms<sup>-1</sup>, momentum flux varies by at least 6% more than the variation expected from current-relative winds alone, and suggests that wave-current interactions can generate significant spatial and temporal variability in momentum fluxes in this region of prevailing trade winds. Results and data from this study motivate the continued development of fully coupled atmosphere-ocean-wave models.

**Plain Language Summary** Six surface current-following drifters were deployed in the northwestern tropical Atlantic during the Atlantic Tradewind Ocean-atmosphere Mesoscale Interaction Campaign to study how surface current gradients influence wave properties. In theory, when spatial variability in currents exists, surface currents are in the opposite direction as the waves will cause a shift in wave frequency and shoaling of wave energy, leading to wave steepening. Increased wave slopes, due to opposing surface currents, may lead to increased whitecapping and wave breaking. Conversely, surface currents in the same direction as the waves are expected to flatten waves. Wind directions were relatively constant, owing to prevailing trade winds. Wave slopes varied by up to 10% at a given wind speed due to the variability of surface currents. This suggests that surface current variability may influence air-sea exchanges of gas, heat, and momentum through their interaction with waves. The effect of surface current variations on waves is often not incorporated into model parameterizations, so these findings may be useful in the development of more fully coupled atmosphere-ocean-wave models.

## 1. Introduction

### 1.1. Importance and Background

Air-sea interactions are an important component of the global climate system, as they modulate the transfer of heat, buoyancy, momentum, and gases between the atmosphere and the ocean and are a driving force behind creating boundary layer to multidecadal-scale patterns in weather and climate. Surface gravity waves are a key component of the air-sea interface and modulate the transfer of momentum from the atmosphere to the ocean through the modification of surface drag (e.g., Janssen, 1989, and others), energy injection from breaking (e.g., Craig & Banner, 1994, and others), and momentum storage in the wave field (e.g., Ardhuin et al., 2004; Fisher et al., 2017, and others). Existing work on the role of waves in air-sea interaction often parameterizes this process using a wind speed-dependent drag coefficient (Edson et al., 2013; Large & Pond, 1981; Smith, 1980) or incorporates waves only through a wave age parameterization, which has been found to produce similar results as parameterizations incorporating wind speed alone (Edson et al., 2013). While these assumptions may be reasonable when waves are modified only by wind and when wind-wave equilibrium (Phillips, 1985) holds, significant uncertainties exist when other processes affect surface waves. A primary objective of the present study is to

© 2022 The Authors.

This is an open access article under the terms of the [Creative Commons Attribution-NonCommercial License](https://creativecommons.org/licenses/by/4.0/), which permits use, distribution and reproduction in any medium, provided the original work is properly cited and is not used for commercial purposes.

evaluate the significance of wave-current interactions, which are not typically incorporated into model parameterizations on wave properties and momentum flux at small scales. Another focus is to compare observations with momentum flux calculated using the COARE bulk flux algorithm (Edson et al., 2013; Fairall et al., 1996, 2003), a widely used scheme that incorporates current and wave effects on stress through current-relative winds and wave age, respectively, but does not parameterize wave-current interactions. It is well documented that surface currents vary at the mesoscale and smaller scales due to eddies and fronts (e.g., Ebuchi & Hanawa, 2000; Kim, 2010; McWilliams, 2016; Molinari et al., 1981; van Aken, 2002; and others); presumably, these current variations would lead to spatial differences in wave-current interactions and momentum flux.

In theory, when waves propagate over an area with spatially varying surface currents, a Doppler shift will modify the apparent wave frequency and effective rate of wave energy propagation by an amount dependent on the alignment of the surface current and the waves. Because the horizontal wave energy flux is conserved along a ray path, changes in the rate of energy propagation cause changes in the local energy density (much like the shoaling process in shallow water). The net effect is to elevate wave slopes when surface current gradients are opposed to wave propagation, and decrease wave slopes when surface current gradients follow wave propagation. The frequency shift is caused by the projection of the current vector onto the wave direction; this component will hereinafter be referred to as the wave-relative current. In areas where currents are spatially variable such as across fronts, wave slopes would be expected to vary on those same spatial scales. This has been observed in the field (Branch et al., 2018; Gemmrich & Pawlowicz, 2020; Kastner et al., 2018; Thomson et al., 2014; Zippel & Thomson, 2017) and simulated by numerical models (Akan et al., 2017, 2018; Moghimi et al., 2019) in coastal areas where strong spatial current variability exists. Specifically, energy levels, significant wave height, whitecapping, wave breaking, and near-surface turbulent dissipation rates are elevated where currents oppose the waves due to wave steepening. Wave properties can vary on spatial scales by ones to tens of km (e.g., Branch et al., 2018; Thomson et al., 2014) or larger (e.g., Gemmrich & Pawlowicz, 2020), depending on the structure of coastal features associated with current variability, including river plumes (Branch et al., 2018; Thomson et al., 2014), fronts, and upwelling jets (Romero et al., 2017). Near river mouths, currents can even be strong enough to reduce the wave group velocity to zero and block the propagation of waves on the side of a front where currents strongly oppose the waves (Chawla & Kirby, 2002; Chen & Zou, 2018).

Only a limited amount of research on wave-current interactions has focused on the open ocean, where currents are typically more wind and wave following than in localized coastal areas. Romero et al. (2017) quantify current effects on wave properties associated with the Loop Current in the Gulf of Mexico. Strong fronts with surface current gradients of up to  $1.5 \text{ ms}^{-1}$  over roughly 50 km exhibited variations in wave height and slope of up to 30%, with greater variation in whitecap coverage. At O (100 km) scales, storms and western boundary currents have been shown to modulate wave properties in the presence of strong surface currents (Hegermiller et al., 2019; Holthuijsen & Tolman, 1991; Wang & Sheng, 2016). Wave-current interactions in the open ocean have also been shown to vary temporally due to varying inertial and tidal currents (Gemmrich & Garrett, 2012). Finally, as in coastal areas, current variations on very small scales can occur in the open ocean: Rasche et al. (2017) observed sea surface roughness anomalies across a 50 m-wide submesoscale front and attribute this to strong current gradients of  $0.3 \text{ ms}^{-1}$ . These results demonstrate that wave-current interactions associated with strong surface current variability are important in the open ocean as well as coastal areas.

Wave-current interactions have been frequently studied using models. Mesoscale features on O (10–100 km scales) cause variations in wave properties through refraction, the advection of energy, the energy exchange between waves and currents, the aforementioned Doppler frequency shift, and the effect of currents on the wind stress between the ocean and atmosphere (Ardhuin et al., 2017). Romero et al. (2020) quantify some of this variability on O (1–10 km scales) with numerical modeling, and demonstrate that wave-current interactions most significantly influence wave-breaking variables including whitecap coverage and energy dissipation, particularly when winds are weak. Wave-current interactions also have a strong influence on significant wave height at scales of tens of kilometers (Ardhuin et al., 2017; Kudryavtsev et al., 2017; Quilfen et al., 2018). Similar effects on significant wave height have been shown at the mesoscale and at larger scales: Quilfen and Chapron (2019) show that current variability on scales of hundreds of kilometers can influence wave heights and Rapizo et al. (2018) show wave flattening on even larger scales due to wave-following currents. Nonnegligible effects of currents have been observed on other bulk wave variables including wave mean square slope (Rasche et al., 2014; Romero et al., 2020). Current effects on waves should theoretically be more significant for wind waves having

frequencies above the spectral peak (McWilliams, 2018; Phillips, 1984). While not the focus of the present study, it has been demonstrated that the reverse feedback can occur as well that is, waves can cause variations in surface currents (McWilliams, 2018; Suzuki et al., 2016; Tang et al., 2007). However, model results have shown that this effect is only a small contributor to submesoscale and mesoscale variability (Romero et al., 2021). Hereinafter in this manuscript, “wave-current interactions” will refer to current effects on waves, rather than wave effects on currents. A main objective of the present study is to analyze the influence of wave-current interactions on short temporal scales and spatial scales of tens of kilometers with observations. This is of similar scale to several previous modeling studies (e.g., Ardhuin et al., 2017; Romero et al., 2020), but smaller than the focus of large-scale observational studies (e.g., Holthuijsen & Tolman, 1991).

In areas with significant mesoscale or submesoscale activity, spatial gradients in currents are often associated with sea surface temperature (SST) fronts. SST fronts can generate spatial variations in air-sea heat fluxes, which can in turn modify momentum fluxes, wind, and waves. For instance, heating over the warm side of a front destabilizes the atmospheric boundary layer, which induces atmospheric convection and increases surface wind speeds through either downward momentum transfer (Wallace et al., 1989) or horizontal pressure gradients (Lindzen & Nigam, 1987). These increases in wind speed can then influence the high frequency part of the wave spectrum. The modification of air-sea fluxes by SST fronts has been observed and modeled at the submesoscale (Redelsperger et al., 2019; Shao et al., 2019) and at the mesoscale (Businger & Shaw, 1984; Chelton et al., 2001, 2004; Friehe et al., 1991; Gaube et al., 2015). The primary focus of this work will be direct effects of the currents on waves and momentum flux, but it is important to note that indirect effects such as those induced by SST fronts may also be significant.

## 1.2. Theory

We expect mss to vary as a result of currents opposing or following the waves, which will further influence surface stress (i.e., momentum flux). We know that

$$\tau = \rho_a u_*^2, \quad (1)$$

where

$$u_* = C_D^{1/2} (U_{10} - U \cos \theta). \quad (2)$$

Parameter  $\tau$  is the surface wind stress,  $\rho_a$  is the air density,  $u_*$  is the friction velocity,  $C_D$  is the drag coefficient,  $U_{10}$  is the 10 m wind speed,  $U$  is the surface current, and  $\theta$  is the angle between the surface current direction and the average wave direction in an equilibrium frequency range ( $f_{\max} - f_{\min}$ ). Assuming that the source of wave energy (i.e., wind) is balanced by wave breaking and nonlinear effects (Phillips, 1984, 1985), and that the wind energy input is proportional to  $u_*$  and mss (Plant, 1982),  $u_*$  can be defined as a function of the wave energy spectrum  $E(f)$ , which scales with  $f^{-4}$  (Juszko et al., 1995; Phillips, 1985; Thomson et al., 2013; Voermans et al., 2020). Within the equilibrium frequency range,

$$u_* = \int_{f_{\min}}^{f_{\max}} \frac{E(f) f^4 2\pi^3}{\beta I(p) g (f_{\max} - f_{\min})} df. \quad (3)$$

Parameter  $f$  is the wave frequency,  $\beta$  is an empirically determined constant taken as 0.012,  $g$  is gravitational acceleration, and  $I$  is the wave directional spreading function with parameter  $p$  as defined by Phillips (1985). Following Phillips (1985), we assume a constant  $p = 0.5$  and  $I(p) = 2.5$ . By combining the above equation with a version of the relation of Kitaigorodskii (1983) that is normalized by the frequency width,

$$mss = \int_{f_{\min}}^{f_{\max}} \frac{E(f) f^4 16\pi^4}{g^2 (f_{\max} - f_{\min})} df, \quad (4)$$

$u_*$  can be related to mss as

$$\frac{u_*}{mss} = \frac{g}{8\pi\beta I(p)}. \quad (5)$$

Hereinafter,  $mss$  will refer to this frequency-width-normalized value rather than the unnormalized value to remove dependence on the selected equilibrium range. Equation 5 demonstrates that  $mss$  and  $u_*$  are directly proportional under the assumptions that  $\beta$  and  $I(p)$  are constant and that there is an equilibrium frequency range  $f_{max} - f_{min}$ . The present study makes these assumptions, so observations presented in terms of  $mss$  and  $u_*$  are essentially equivalent and differ only by a constant factor. This wave-derived  $u_*$  is distinct from estimates based on anemometer measurements (whether bulk or turbulent), but it is meant to be the same dynamic quantity.

When waves encounter a uniform current in the same or opposite direction as the waves, the Doppler shift effect leads to a shift in wave frequency by an amount proportional to wavenumber and the component of the current velocity aligned with the waves (Phillips, 1984). This frequency shift can be defined using

$$\omega = \sigma + \vec{u} \cdot \vec{k} = \sigma + U k \cos(\theta), \quad (6)$$

where  $\omega$  is the absolute frequency of the wave in a fixed reference frame and  $\sigma$  is the intrinsic frequency defined with the deep-water wave dispersion relation,

$$\sigma = 2\pi f = \sqrt{gk}. \quad (7)$$

Parameter  $\vec{u}$  is the current and  $\vec{k}$  is the wavenumber. Currents opposing the direction of wave propagation will cause an increase in wavenumber and decrease in the rate of energy propagation. When a wave-relative current  $U \cos\theta$  is imposed, the surface energy flux of the waves  $F_{waves}$  is defined as

$$F_{waves} = E(f) \times (c_g(f) + U \cos\theta), \quad (8)$$

where  $E$  is the local energy density and  $c_g(f) = \frac{g}{4\pi f}$  is the deep-water group velocity. To conserve  $F_{waves}$  when  $U \cos\theta$  is negative,  $E$  must increase and the waves will steepen. This process is different for each frequency  $f$  in a given spectrum, because  $c_g(f)$  is a strong function of frequency. The high-frequency components (which determine  $mss$ ) have the largest effective change in the rate of energy propagation for a given  $U \cos\theta$ .

If waves reach a critical steepness, they can break (Gemrich & Pawlowicz, 2020; Phillips, 1984; Romero et al., 2017; Thomson et al., 2014; van der Westhuysen, 2012; Zippel & Thomson, 2017). Similarly, currents in the same direction as the waves will experience a decrease in wavenumber, increase in wave speed, and flattening. Wave properties are further modified when strong vertical (Banihashemi et al., 2017; Banihashemi & Kirby, 2019; Choi, 2009; Ellingsen & Li, 2017) or horizontal (Haus, 2007) current shear exists. To account for the current effect on wave frequency in a field with variable currents, we substitute the absolute frequency  $\omega$  (Equation 6) for  $f$  in Equation 4. This yields a relationship between  $mss$ , the intrinsic frequency  $\sigma$ , the wavenumber  $k$ , and the wave-relative current  $U \cos\theta$ . Combining this with the dispersion relation (Equation 7), we can rewrite  $\sigma$  and  $k$  in terms of  $f$  and obtain an equation for the frequency width-normalized  $mss$  (or equilibrium  $u_*$ , using Equation 3),

$$mss = \int_{f_{min}}^{f_{max}} \frac{16\pi^4 f^4 E(f)}{g^2 (f_{max} - f_{min})} \left( 1 + \frac{8\pi f U \cos\theta}{g} + \frac{24\pi^2 f^2 (U \cos\theta)^2}{g^2} + \frac{32\pi^3 f^3 (U \cos\theta)^3}{g^3} + \frac{16\pi^4 f^4 (U \cos\theta)^4}{g^4} \right) df, \quad (9)$$

as a function of  $U \cos\theta$  and  $E(f)$ , which is expected to increase at increasing wind speeds (Equations 2 and 3). Using Equation 9, we can calculate an expected variation in  $mss$  or  $u_*$  when a nonzero uniform current  $U$  is imposed at an angle  $\theta$  to the wave direction.

The theory suggests that the relative surface current would also contribute to variability in  $u_*$ , both by modifying the current-relative wind speed ( $U_{10} - U \cos\theta$  in Equation 2; Figure 1a) and through wave-current interactions. It is important to note that while these two mechanisms both result from surface currents, they are physically distinct. Surface currents will influence the current-relative wind speed and  $u_*$  regardless of spatial variability. That is, in a hypothetical ocean where surface currents are spatially invariant but nonzero,  $u_*$  will still be increased or decreased compared to a case where surface currents are zero. On the other hand, wave-current interactions only occur in the presence of spatial variability. A wave has to propagate across an area of spatially varying surface currents for the Doppler shift and conservation of wave energy flux to alter the wave steepness. The

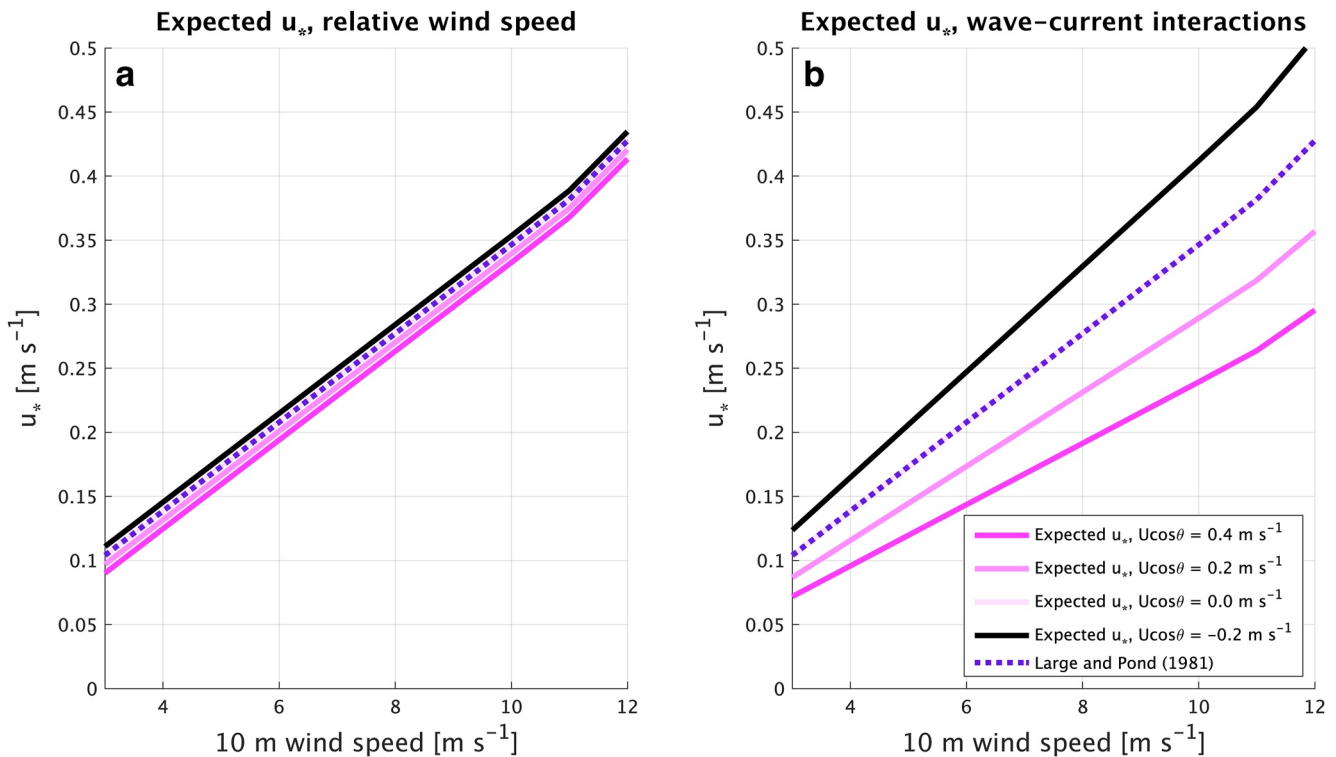


**Figure 1.** (a) Expected variation in  $u_*$  due to the direct effect of currents, assuming  $C_D$  from Large and Pond (1981) (current-relative wind, Equation 2); (b) Expected variation in  $u_*$  due to wave-current interactions (Equations 5, 8, and 9).

analysis in this manuscript discusses both of these processes and often makes the assumption that because data were collected in a region where winds are consistently from the same direction, deviations in currents from the strongly wind-following direction are associated with spatial variability.

A recent study estimated wind speed from in situ observations of wave spectra and found that observed wind speeds between 3 and 12  $\text{m s}^{-1}$  are generally consistent with values predicted from Equation 3, with uncertainty resulting from sea state and buoy motion (Voermans et al., 2020). While wave properties vary significantly due to the Doppler shift effect in coastal regions where surface currents are strong and variable (Campana et al., 2016; Gemmrich & Pawlowicz, 2020; Thomson et al., 2014; Zippel & Thomson, 2017), the influence of wave-current interactions on  $u_*$  has not been explored in the open ocean using observations, with the exception of areas with strong mesoscale activity and current variations (Hegermiller et al., 2019; Holthuijsen & Tolman, 1991; Romero et al., 2017). The theory suggests that even small spatial changes in surface currents will have nonnegligible effects on  $u_*$  (Figure 1b), so wave-current interactions may still be important in locations away from coastal areas or major western boundary currents. Furthermore, areas without strong mesoscale activity are more representative of the global ocean as a whole. A goal of the present study is to evaluate the impact of wave-current interactions in a region of moderate mesoscale activity (Figure 2).

## 2. Methods

### 2.1. Study Site

The NOAA Atlantic Tradewind Ocean-atmosphere Mesoscale Interaction Campaign (ATOMIC), part of EUREC<sup>4</sup>A (Stevens et al., 2021), took place in January-February 2020 in the northwestern tropical Atlantic, east-northeast of Barbados (Figure 2). This region is north of the intertropical convergence zone and well within the trade wind region. As a result, wind and waves are typically strong and westward following the prevailing trade winds, with minimal directional variation. The ATOMIC study site is also adjacent to a region that has strong oceanic mesoscale activity (Figure 2) and spatial variability in ocean temperature and salinity: The outflows of the Amazon and Orinoco Rivers are nearby and large mesoscale ocean eddies are generated by the



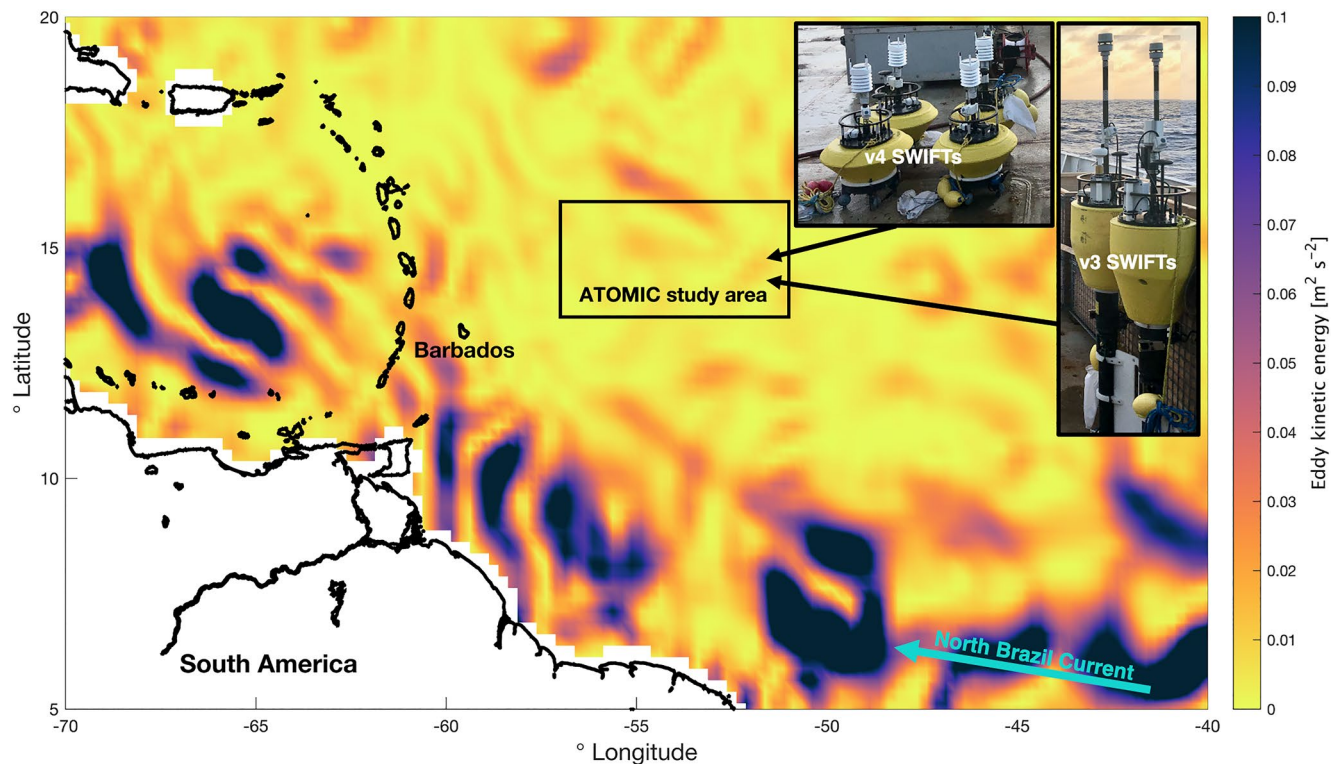


**Figure 2.** Eddy kinetic energy calculated from Copernicus Marine Environment Monitoring Service satellite sea level anomalies on 1 February 2020. The rectangular box denotes the study area where Surface Wave Instrument Float with Trackings (SWIFTs) were deployed and recovered. Inset images picture the two types of SWIFTs deployed during Atlantic Tradewind Ocean-atmosphere Mesoscale Interaction Campaign.

North Brazil Current (Ffield, 2005; Fratantoni & Glickson, 2002; Fratantoni & Richardson, 2006). Despite this, only moderate eddy kinetic energy was observed during the field campaign (Figure 2) because the study site is farther north than the region of highest eddy kinetic energy and freshwater discharge (Reverdin et al., 2021) and the field campaign took place before the boreal spring peak discharge (Coles et al., 2013). However, river outflow or mesoscale eddies are still likely responsible for the observed submesoscale spatial variability in the ATOMIC study area (Figure 2).

## 2.2. SWIFT Observations

During the ATOMIC field campaign, two version 3 (v3) Surface Wave Instrument Float with Tracking (SWIFT) drifters (Thomson, 2012) and four version 4 (v4) SWIFT drifters (Thomson et al., 2019) were deployed. The field campaign consisted of two cruise legs on the NOAA Ship Ronald H. Brown (Quinn et al., 2021) and 11 NOAA P-3 aircraft flights (Pincus et al., 2021) from Barbados to the study area shown in Figure 2. SWIFT drifters were deployed twice from the NOAA Ship Ronald H. Brown from 14 January 2020 to 22 January 2020 during Leg 1 and from 30 January 2020 to 11 February 2020 during Leg 2. Leg 1 deployments were made in the northeastern part of the study area and Leg 2 deployments were made in the southwestern part of the study area. Details of these deployments and other measurements that were made during ATOMIC from the NOAA Ship Ronald H. Brown or other oceanic platforms are included in Quinn et al. (2021).

During both legs of ATOMIC, ocean temperature fronts were identified using satellite measurements and ship-board sensors. SWIFTs were then strategically deployed in a line across the front, with 5–10 km spacing between each drifter's initial deployment positions. This strategy ensured that significant spatial variability in ocean temperature and surface currents was observed during the beginning of each deployment. Toward the end of deployments, SWIFT drifters converged to one (leg 1) or two (leg 2) general geographic areas due to currents.

V3 and v4 SWIFTs differed in height and had instrumentation at different heights and depths. V4 SWIFTs were equipped with Vaisala WXT350 meteorological sensors at 0.5 m height, which measured parameters including

air temperature, relative humidity, and wind speed and direction. V3 SWIFTS were equipped with Airmar 200WX meteorological sensors at 0.8 m height, which measured the above parameters excluding relative humidity. Aanderaa 4319 sensors measured conductivity and ocean temperature at 0.3 m depth on v4 SWIFTS and at 0.5 and 1.0 m on v3 SWIFTS. Nortek Signature 1000 (v4) or Nortek Aquadopp (v3) ADCPs measured ocean current velocities between 0.35 and 20 m depth. Directional wave spectra and bulk wave parameters were estimated from inertial motion observations on both v3 and v4 SWIFTS using a Microstrain 3DM-GX3-35 (v3) or SBG Ellipse (v4) attitude and heading reference system (AHRS). These systems also included GPS measurements, with wave spectral processing as described in Thomson et al. (2018). Raw data were processed onboard, and spectral results were sent via Iridium telemetry once per hour, corresponding to a 10 min burst of raw data at the top of each hour.

### 2.3. Data Processing

Offsets in wind speed measurements were calibrated using shipboard observations made when a drifter was within 5 km of the ship by assuming that ship and drifter observations should be identical and performing linear regressions for each platform (Thomson et al., 2021). If fewer than 5 collocated data points were available for a given regression, offsets were first corrected using observations from another drifter that was near the ship. For one v4 drifter, a distance limit of 15 km was used because of a lack of data from other drifters closer than that. Root mean square errors in offsets were generally lower than sensor precision specifications; wind speed observations from individual SWIFTS had uncertainties between 0.24 and 0.96  $\text{ms}^{-1}$ .

SWIFT drifters are nearly Lagrangian surface-following platforms (Thomson, 2012), which drift with the surface currents. Surface currents are estimated from the drift track of SWIFTS, after subtracting the contributions from Stokes drift (following the methods of Thomson et al. (2019)) and wind slip. Stokes drift corrections are small ( $\text{cms}^{-1}$ ) relative to the surface currents. Drifter slip (i.e., offset between the platform motion of near-Lagrangian drifters and the actual currents) typically is the result of drifter windage and near-surface velocity shear (Niiler & Paduan, 1995; Poulain et al., 2013). As shear was minimal (discussed in detail later in this section), we assume that drifter slip is primarily a result of windage. Following Herrera et al. (2019), slip was calculated using onboard ADCP velocity observations made in the reference frame of the drifter. Because shear was minimal, velocities at 0.85 m depth were representative of the depth-averaged relative platform velocity and were used for this calculation. In theory, onboard velocities should be zero if drifters drift with the near-surface currents. Any nonzero velocity represents the difference between the drift and the current velocity. Moderate correlation ( $R^2 = 0.37$ ) between wind speed and ADCP velocities supports the assumption that slip is a result of wind. Wind slip was, on average, 1.09% of the wind speed, with a standard deviation of 0.27%. To correct surface currents for wind slip, a vector with magnitude of 1.09% of the wind speed in the direction of the wind was subtracted from Stokes-corrected drift tracks. When wind data were unavailable, data from the nearest drifter were used. Wind slip corrections were typically a small northeastward adjustment of 0.05–0.15  $\text{ms}^{-1}$ ; this direction for the adjustment is consistent with the prevailing trade winds.

Wave slopes  $m_{ss}$  and equilibrium  $u_s$  are calculated from wave spectra, assuming a constant equilibrium frequency range over which the source and sink of wave energy is balanced (Equations 3 and 4). (Thomson et al., 2013) define the equilibrium frequency range as between 0.2 and 0.4  $\text{s}^{-1}$ . We slightly modify this range and use  $f_{\min} = 0.25 \text{ s}^{-1}$  and  $f_{\max} = 0.4 \text{ s}^{-1}$  since swell is occasionally observed at frequencies between 0.2 and 0.25  $\text{s}^{-1}$ . Linear fits to the equilibrium range of the spectra in log-log space have an average slope of  $-3.89$  (Figures 3a and 3c), roughly consistent with the theoretical  $f^{-4}$  shape. Minor deviations from the  $f^{-4}$  shape are frequently observed, although spectral slopes in the equilibrium range are rarely less steep than  $f^{-3}$  or steeper than  $f^{-5}$  (Figure 3c). Deviations from the  $f^{-4}$  shape are likely due to noise combined with the limited amount of data (10 min) used to calculate each spectrum.

Spectral shapes at high frequencies may be modulated by swell waves (Vincent et al., 2019) or coupling between the swell and high frequencies (Collins et al., 2018); when swell is strong (high wave centroid periods), spectral slopes are typically steeper than  $f^{-4}$  (Figure 3c). The transition between the equilibrium ( $f^{-4}$ ) and saturation ( $f^{-5}$ ) subranges has also been shown to be shifted to lower frequencies when  $u_s$  is high (Lenain & Melville, 2017). Sensitivity tests involving calculating  $m_{ss}$  and equilibrium  $u_s$  using an equilibrium frequency range prescribed based on the wave peak frequency (i.e., as done by Banner, 1990), centroid frequency, or wave age produce results

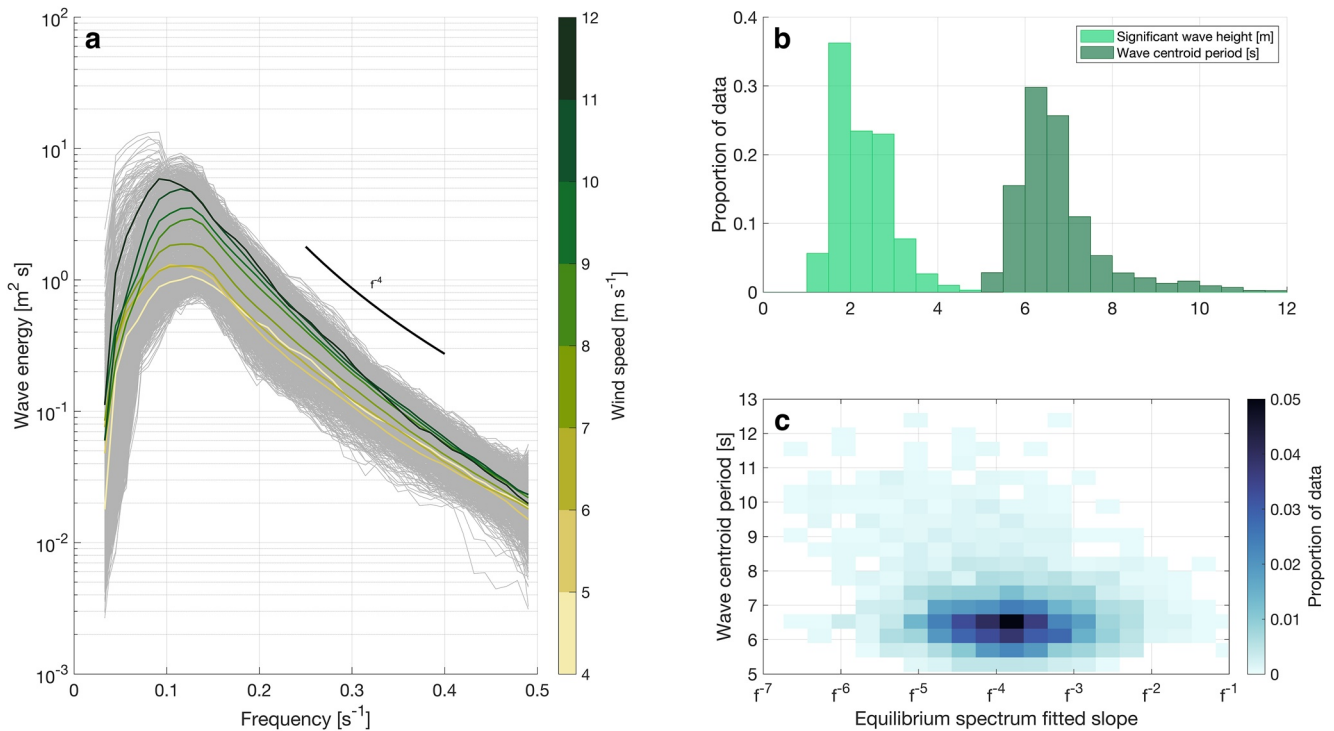


**Figure 3.** (a) Wave spectra observed from v4 Surface Wave Instrument Float with Tracking drifters during both legs of Atlantic Tradewind Ocean-atmosphere Mesoscale Interaction Campaign. Energy at individual frequencies was smoothed over a 3-hr time period and in frequency space over  $0.059 \text{ s}^{-1}$  (gray;  $n = 1156$ ). Colored lines denote average spectra within  $1 \text{ ms}^{-1}$ -wide wind speed categories. Spectra with a wave direction of  $<0^\circ$  or  $>150^\circ$  had significant swell input and are excluded. (b) Histograms of significant wave height and wave centroid period from all drifters. (c) Binned scatter plot of wave centroid period versus fitted equilibrium range spectral slope for all drifters.

that are negligibly different from the above method (not shown). Removing spectra with significant deviations from the  $f^{-4}$  shape (Figure 3c) also has minimal influence on the overall results.

Near-surface vertical shear is a potential source of uncertainty in surface wave-relative current estimates. ADCP velocity observations below 0.35 m (not shown) demonstrate that the velocity difference between 0.35 and 15 m depth is typically only around  $0.05 \text{ ms}^{-1}$ , which is small compared to the range of surface wave-relative currents observed (Figure 4c). Kirby and Chen (1989), Zippel and Thomson (2017) and others showed that wave-current interactions are dependent on the spatial scale of the waves. Waves with a frequency between 0.25 and  $0.4 \text{ s}^{-1}$  will have a wavelength between 10 and 25 m, assuming deep-water wave dispersion. These waves will thus be sensitive to currents on vertical scales of 5–10 m, approximately half their wavelength (Kirby & Chen, 1989; Zippel & Thomson, 2017). Hence, although significant current shear has previously been observed above 0.35 m (e.g., Laxague et al., 2018), this shear near the surface likely only minimally influences wave-current interactions in the selected frequency range.

Wave directions are calculated using directional moments and the maximum entropy method (Lygre & Krogstad, 1986). For consistency with the mss observations, the averaged value in the equilibrium range is used as the wave direction. An energy-weighted average direction was also calculated, but rarely differed by more than  $10^\circ$  from the average direction and thus was not used. mss, equilibrium  $u_{*s}$ , and wave direction data are smoothed over 3-hr periods because each individual spectrum consists of only 10 min of data (12 degrees of freedom), which is not enough to obtain robust estimates of wave parameters. For consistency, all other atmospheric and oceanic observations are smoothed over 3-hr periods. In general, when winds are higher, waves are more energetic (Figure 3a). This leads to greater mss (Equation 4). An objective of the present study is to isolate the dominant effect of wind speed on spectral energy in order to evaluate a secondary effect, in which opposing or following surface currents influence spectra and mss through wave-current interactions.



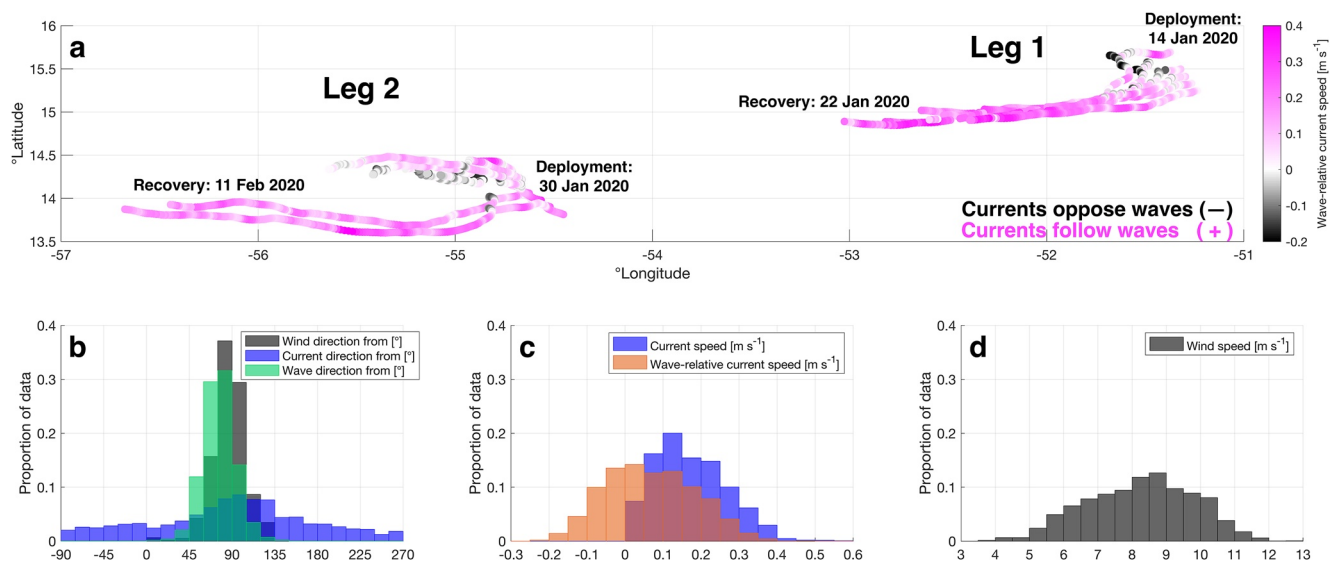


**Figure 4.** (a) Drift tracks of all Surface Wave Instrument Float with Tracking drifters during both legs of Atlantic Tradewind Ocean-atmosphere Mesoscale Interaction Campaign. Colors represent the component of the current vector aligned with the waves. Histograms of data from all drifters: (b) wind ( $v_3$  only), wave, and current direction (note that green-gray indicates overlap of wind and wave directions, dark blue indicates overlap of wind and current directions, light blue-green indicates overlap of wind and wave directions, and dark blue-green indicates overlap of wind, wave, and current directions); (c) current and wave-relative current speed; (d) wind speed.

Data collected during a large swell event that occurred from 19 to 21 January 2020 are excluded from further analysis because of the effect of swell waves on the wave directional spectra in the equilibrium range. First, when swell is strong, high frequency wave directions are shifted away from the wind direction, leading to a much larger directional spread. Because wave energy is spread over a wide directional range, it is difficult to determine the direction aligned with the currents that would be expected to be most significantly influenced by wave-current interactions. Second, swell is associated with elevated energy levels between 0.25 and 0.3  $\text{s}^{-1}$ , which leads to spectral slopes that are consistently steeper than  $f^{-4}$  (Figure 3c) and therefore inconsistent with equilibrium theory. Swell modulation of the mid-to high-frequency portion of the wave spectrum, including shifting the transition frequency between the equilibrium and saturation subranges, has previously been observed (Vincent et al., 2019). To exclude conditions where swell significantly influenced high-frequency energy levels, we only analyze data where the average wave direction in the equilibrium range is  $>0^\circ$  and  $<150^\circ$ , as high frequency wave directions during the swell event were typically  $150^\circ$ – $300^\circ$ . This criterion eliminates data almost exclusively from the 19–21 January 2020 swell event, which comprise  $<6\%$  of all observations. Because wind direction does not significantly vary in the ATOMIC region, this technique is analogous to the spectral partitioning method of Portilla et al. (2009).

$V_3$  SWIFTs are larger in size and much taller than  $v_4$  SWIFTs (Figure 2 inset) and thus susceptible to bias at high frequencies due to tilting at high wind speeds. To account for this, mss observations from each  $v_3$  SWIFT are corrected using data from  $v_4$  SWIFTs. This is done by comparing mss observations from  $v_3$  and  $v_4$  SWIFTs when a  $v_4$  SWIFT was within 20 km of the  $v_3$  SWIFT. Linear regressions of wind speed versus mss are then developed to relate  $v_3$  and nearby  $v_4$  data, and  $v_3$  data are corrected by subtracting the difference between the linear fits at each wind speed. Potential uncertainty in the corrections due to spatial variability in the wave field is further discussed in the following paragraph. On average, this correction decreases mss by  $1.5 \times 10^{-3}$ , or 6.2%, with slightly larger corrections at higher wind speeds. A sensitivity test that involved recalculating mss and  $u_*$  without making this correction (not shown) determined that correcting the tilting bias has little effect on the results presented in subsequent sections.

Data processing techniques used to correct wind speed and  $v_3$  mss measurements involved using observations from closely spaced platforms to develop a linear relationship used to make corrections. As highlighted in this manuscript, spatial variations likely exist on small scales, so observations from nearby drifters are not always equivalent for individual data pairs. However, this correction method is reasonable for several reasons: First,

many pairs of drifters were much closer together than the stated criterion; for instance, v4 drifters used to correct mss from v3 drifters were only 10.8 km apart on average. Second, large amounts of data ( $n = 598$ ) are used to calculate the relationships used to correct v3 mss. Third, variations in mss due to wave-current interactions or other intermittencies in the wave field are not more frequently observed by v3 or v4 drifters (i.e., steeper waves due to opposing surface currents would be observed at the same frequency by v3 and v4 drifters). Because of this, the spatial variability between drifters, a source of random error, is smoothed out when constructing regressions. Finally, in the individual case with significant spatial variability highlighted in Section 3.2.2, variability is on scales of over 20 km and hence a correction on smaller scales would not influence those results.

### 3. Results

We first evaluate the range of wind, wave, and current conditions observed during ATOMIC (Section 3.1). We then evaluate how mss and equilibrium  $u_*$  differ across different current conditions in case studies on varying spatial scales (Section 3.2) and collectively in the study area (Section 3.3). Results are reported in Section 3.2 in terms of mss to highlight the effect of wave-current interactions on wave slope, while results are discussed in Section 3.3 in terms of  $u_*$  to highlight the effects on friction velocity and air-sea momentum flux. We reiterate that reported mss and  $u_*$  are directly proportional assuming that an equilibrium spectrum exists: if  $f_{\max} - f_{\min} = 0.15 \text{ s}^{-1}$ ,  $\beta = 0.012$ , and  $I(p) = 2.5$ ,  $u_*$  will be higher than mss (normalized by frequency width) by exactly a factor of  $13.0 \text{ ms}^{-1}$  (Equation 5).

#### 3.1. Wind, Wave, and Current Conditions During ATOMIC

Wind directions during ATOMIC were typically from the east or northeast following the prevailing trade winds. Wind speeds were variable: observed values ranged from  $3.7 \text{ ms}^{-1}$ – $13.0 \text{ ms}^{-1}$  with a mean of  $8.2 \text{ ms}^{-1}$  and a standard deviation of  $1.6 \text{ ms}^{-1}$  (Figure 4d). Variations in wind speed led to variations in significant wave height. Significant wave heights averaged 2.3 m with a standard deviation of 0.6 m (Figure 3b), but were elevated to over 4 m during the swell event on 19–21 January 2021. Significant wave height was positively correlated with wave period; a mean wave centroid period of 6.8 s was observed, but this value increased to over 9 s during the swell event. As discussed previously, we exclude data from this period of time. Wave directions in the equilibrium frequency range were within  $\pm 20^\circ$  of the wind direction 78% of the time (Figure 4b). Surface ocean current directions were usually aligned with the wind and waves, but had significantly greater variability. Currents were westward and aligned (within  $\pm 90^\circ$ ) with the waves 68% of the time (Figures 4a–4c). Currents opposed the waves ( $> 90^\circ$  angle between wind and wave directions) 32% of the time. Current speeds were on average  $0.17 \text{ ms}^{-1}$ , with a standard deviation of  $0.11 \text{ ms}^{-1}$ . The vector component of the current aligned with the waves (i.e., the wave-relative current) varied between  $-0.24 \text{ ms}^{-1}$  and  $0.47 \text{ ms}^{-1}$ , with an average of  $0.07 \text{ ms}^{-1}$  and a standard deviation of  $0.12 \text{ ms}^{-1}$ .

As discussed previously, SWIFT drifters are Lagrangian platforms which follow the surface currents (with small additional contributions from wind slip and Stokes drift). Drifters often made loops and turns due to current variability on timescales of under 24 hr (e.g., see Figure 5a). This is considerably shorter than the inertial period, so these features are likely fronts or filaments rather than inertial oscillations. Surface current variability is especially apparent during Leg 2: Currents were slower and highly variable in the northern region with four drifters, and faster and aligned with the wind in the southern region with two drifters (Figure 4a).

#### 3.2. Case Studies

##### 3.2.1. Case 1: Small-Scale Current Loop

Two SWIFTs drifted toward the southwest in the southern part of the study region for a 72-hr period from 0000 UTC on 2 February 2020 to 0000 UTC on 5 February 2020, during the second set of drifter deployments. During this period of time, two other drifters made a clockwise reversing turn in an area of cooler water to the north, on the scale of 10 km. While all drifters generally drifted southwestward, shifts in current direction lasting 12–24 hr caused them to briefly drift eastward. This resulted in the observed loops, on scales of less than 10 km, in the

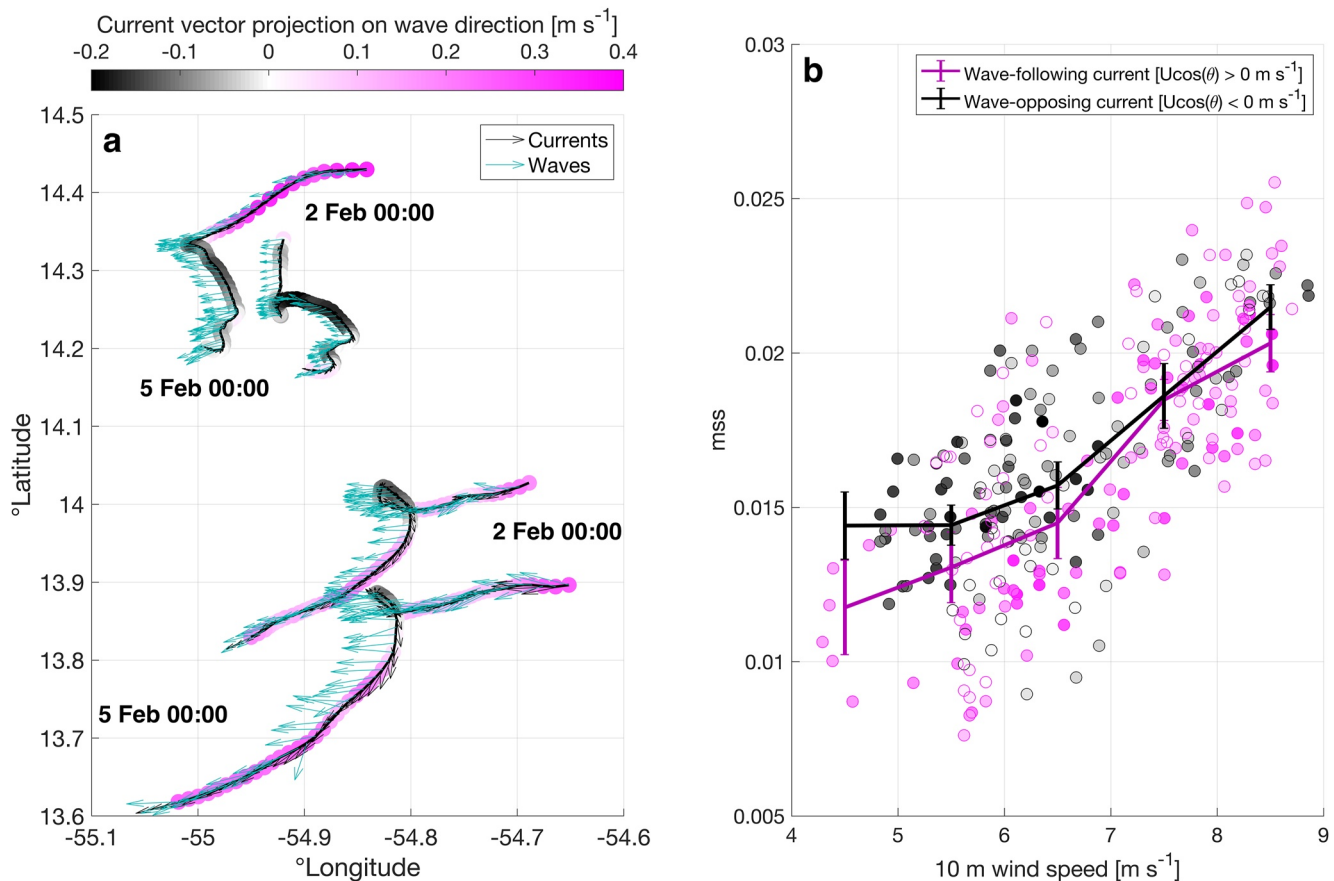


**Figure 5.** Surface Wave Instrument Float with Tracking (SWIFT) observations from Case 1. (a) Drift tracks. Colors represent the component of the current vector aligned with the waves, black quivers represent the current direction, and cyan quivers represent the wave direction. (b) mss versus wind speed for four SWIFT drifters from 2 February 2020 0000 UTC to 5 February 2020 0000 UTC during leg 2 of Atlantic Tradewind Ocean-atmosphere Mesoscale Interaction Campaign. Lines denote averages in  $1 \text{ m s}^{-1}$ -wide wind speed bins, separated by the wave-relative current ( $U \cos\theta$ ). Points are colored by the wave-relative current, with point outlines denoting whether  $U \cos\theta < 0$  (black) or  $U \cos\theta > 0$  (pink). All plotted bins contain a minimum of 10 data points.

drift tracks at  $14.25^\circ\text{N}$  and  $54.82^\circ\text{W}$  in Figure 5a. Wind speeds observed by the southern two drifters steadily decreased from  $9$  to  $4 \text{ m s}^{-1}$  throughout most of the 72-hr period. Wind speeds observed by the northern two drifters were steady around  $4$ – $6 \text{ m s}^{-1}$  for the first 48 hr, before increasing to  $7$ – $9 \text{ m s}^{-1}$  for the remainder of the time period. Throughout the domain, wind and waves were consistently from the northeast without changing direction (Figure 5a). This is expected in a region with prevailing trade winds.

Because wind and wave directions were relatively constant, eastward currents correspond to conditions where the currents and waves were in opposite directions, as seen by the black markers in Figure 5. When currents opposed waves, mss was considerably higher than when currents were aligned with the waves during similar wind conditions (Figure 5b). Specifically, average mss at wind speeds between  $5$  and  $7 \text{ m s}^{-1}$  was 9% higher in opposing current conditions. At wind speeds between  $4$  and  $5 \text{ m s}^{-1}$ , this difference was 20%. Differences were much smaller between  $7$  and  $9 \text{ m s}^{-1}$ , although mss was still greater in wave-opposing conditions compared to wave-following conditions in all five bins. The small difference in mss between current conditions at wind speeds over  $7 \text{ m s}^{-1}$  appears to be because wave-opposing currents were much weaker in these bins than below  $7 \text{ m s}^{-1}$  winds (i.e., the black points in Figure 5b are much lighter at higher winds, denoting only very weakly wave-opposing currents). The average difference in wave-relative current between the wave-following and wave-opposing conditions (pink and black lines in Figure 5b) was  $0.20 \text{ m s}^{-1}$ , which at average wind speeds is expected to be associated with a difference in mss of 3.3% due to the difference in relative winds. This is shown by the difference in  $u_*$  (assumed to be proportional to the difference in mss) between colored lines in Figure 1a. Thus, although differences were not statistically significant at the 95% confidence level except in the  $4$ – $5 \text{ m s}^{-1}$  bin (Figure 5b),

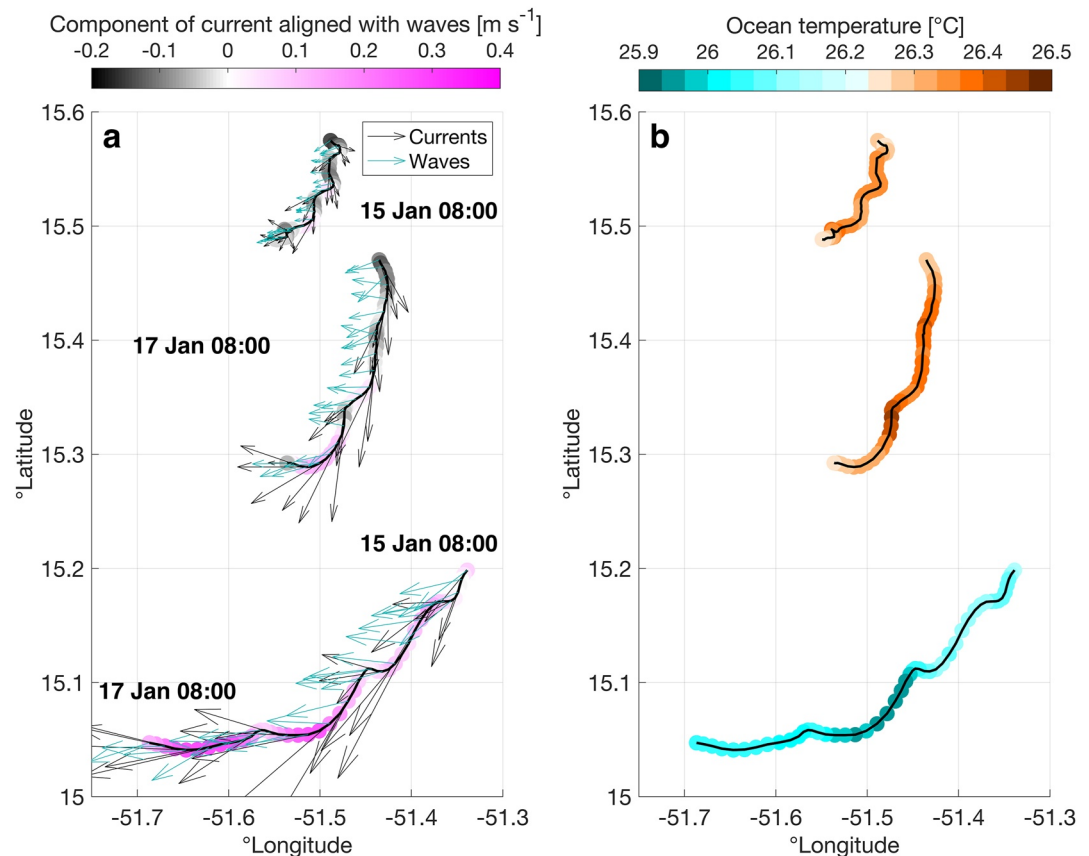


**Figure 6.** Surface Wave Instrument Float with Tracking observations from Case 2, collected from 15 January 2020 0800 UTC to 17 January 0800 UTC during leg 1 of Atlantic Tradewind Ocean-atmosphere Mesoscale Interaction Campaign. (a) Drift tracks. Colors represent the component of the current vector aligned with the waves, black quivers represent the current direction, and cyan quivers represent the wave direction. For clarity, quivers are only plotted every 2 points (hours). (b) Drift tracks. Colors represent near-surface ocean temperature in the top 0.5 m.

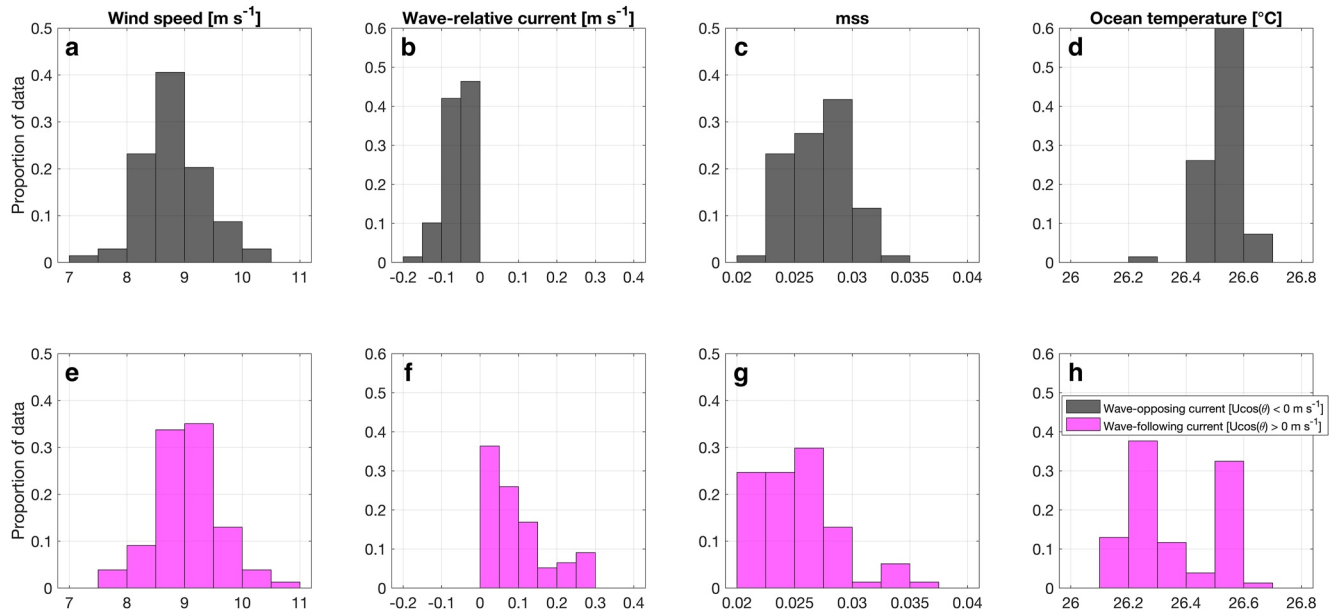
the observed mss still differed by a much greater amount between current regimes than expected from relative winds alone. This suggests that wave-current interactions elevated (suppressed) wave slopes while the surface currents were opposing (following) the waves.

### 3.2.2. Case 2: 30–50 km Front

Three SWIFTs drifted southwestward during a 48-hr period from 15 January 2020 0800 UTC to 17 January 2020 0800 UTC near the start of leg 1 of ATOMIC. A ocean temperature front existed between the southernmost and two northern drifters, as evidenced by a spatial difference in ocean temperature of about  $0.3^{\circ}\text{C}$  (Figure 6b) across 30–50 km. Currents were also considerably faster south of the front, as seen by the long drift track of the southernmost drifter (Figure 6a). Unlike the previous case study, wind speeds were steady at  $8\text{--}10 \text{ ms}^{-1}$  throughout the domain.

Because wind speeds only varied by around  $2 \text{ ms}^{-1}$  during this case study, we evaluate the variability in mss using histograms of wind speed, wave-relative current, mss, and ocean temperature in two wave-relative current regimes: wave-following currents and wave-opposing currents (Figure 7). Wind speeds were, on average, slightly higher when currents followed the waves (Figure 7e). Despite the stronger winds, average mss was considerably lower in these wave-following current conditions (Figure 7g). On the other hand, mss was relatively high, often near  $3.0 \times 10^{-2}$ , when currents opposed the waves (Figure 7c). These results demonstrate that in this case with nearly invariant winds, wave-relative currents were the primary driver in modulating mss. However,





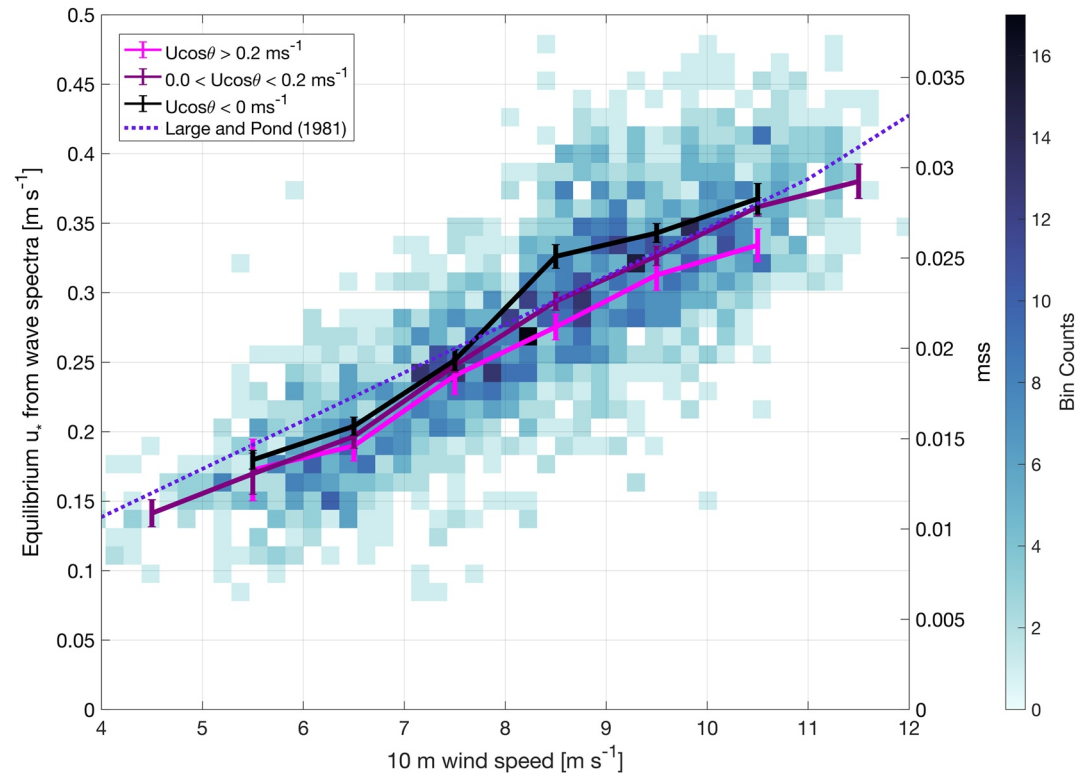
**Figure 7.** Histograms of Surface Wave Instrument Float with Tracking (SWIFT) observations from Case 2: (a and e) wind speed, (b and f) wave-relative current, (c and g) mss, and (d and h) ocean temperature for three SWIFT drifters from 15 January 2020 0800 UTC to 17 January 0800 UTC during leg 1 of Atlantic Tradewind Ocean-atmosphere Mesoscale Interaction Campaign. Colors represent categories of the wave-relative current: Black denotes wave-opposing currents ( $U \cos \theta < 0 \text{ ms}^{-1}$ ;  $n = 69$ ) and pink denotes wave-following currents ( $U \cos \theta > 0 \text{ ms}^{-1}$ ;  $n = 77$ ).

Figure 7g demonstrates that intermittent stronger winds also occasionally elevate mss: several points with wind speeds greater than  $10 \text{ ms}^{-1}$  and mss greater than 0.03 were observed in wave-following current conditions where currents would not be expected to steepen waves. The near-surface ocean temperatures associated with current regimes (Figures 6b, 7d, and 7h) show that wave-following currents were almost exclusively observed south of the temperature front, while opposing currents were more commonly observed by the northern two drifters. These results suggest that the mesoscale temperature front coincided with a front in surface currents that led to spatial variability in wave-current interactions.

### 3.3. Synthesis of all Data

Figure 8 shows the average observed mss and  $u_*$ , computed from Equation 3 using the equilibrium range of the wave spectra, binned by wind speed and separated by wave-relative current conditions for all SWIFT observations during ATOMIC.  $u_*$  derived from wave spectra is generally consistent with the expected values of Large and Pond (1981). This suggests that wind speed and surface stress can be predicted from wave spectra alone and supports the findings of Voermans et al. (2020).  $u_*$  generally increases as wave-relative currents decrease (i.e., currents are more wave opposing). The differences in average mss and  $u_*$  between wave-relative current conditions were statistically significant at the 95% level at most but not all wind speed bins. This may be due to the fact that wind speeds sometimes differed between current conditions even within bins; that is, slightly lower wind speeds observed during wave-opposing current conditions may partially cancel out the effect of currents increasing  $u_*$ . The variability in  $u_*$  between different current conditions generally increases with increasing wind speed, which is consistent with the theoretical predictions based on wave-current interactions shown in Figure 1b and Equations 8 and 9. There are differences in  $u_*$  between different levels of wave-following currents, which suggest that wave-current interactions may be important even when wave-opposing currents are not present, provided that spatial variability exists.

To quantify the effect of wave-current interactions, it is necessary to isolate the effect of currents from the dominant effect of wind speed on  $u_*$ . A multiple linear regression assesses the variability in  $u_*$  independent of wind speed: assuming  $u_*$  depends only on wind speed and wave-relative current, the effect of currents and wind speed on  $u_*$  can be individually quantified. This regression is described by Equation 10,



**Figure 8.** Equilibrium  $u_*$  and mss versus wind speed for all Surface Wave Instrument Float with Tracking data during both legs of Atlantic Tradewind Ocean-atmosphere Mesoscale Interaction Campaign. Lines denote averages in  $1 \text{ m s}^{-1}$ -wide wind speed bins, colored by the wave-relative current ( $U \cos \theta$ ). Error bars represent 95% confidence intervals around the mean of each bin. Blue shading represents the number of observations near a given wind speed and mss or  $u_*$ . All plotted bins contain a minimum of 10 data points. The dotted purple line shows expected values of  $u_*$  calculated from the relationship in Large and Pond (1981).

$$u_* = x + y U_{10} - z U \cos(\theta), \quad (10)$$

which shows the average individual contributions of wind speed ( $U_{10}$ ) and wave-relative current ( $U \cos(\theta)$ ) to  $u_*$ . Using  $u_*$  inferred from the wave spectra and  $U_{10}$  and  $U \cos(\theta)$  from the SWIFT observations, we find that  $x = -0.043 \pm 0.006$  (standard error),  $y = 0.041 \pm 0.001$ , and  $z = -0.084 \pm 0.009$  ( $R^2 = 0.66$ ). The method used to obtain  $u_*$ , using wave spectra calculated from 10-min segments of data, is likely responsible for the relatively low  $R^2$  value, as robust wave statistics cannot be obtained from short bursts. Physically,  $y$  and  $z$  are the contributions of  $U_{10}$  and  $U \cos(\theta)$  to  $u_*$ . The offset  $x$  is likely an artifact of the differences between the moderate- and low-wind relationship between  $U_{10}$  and  $u_*$  (Edson et al., 2013), with additional contribution from the assumption of constant  $\beta$  and  $I(p)$  in calculations of  $u_*$ . We note that using multiple linear regression to calculate Equation 10 inherently assumes that  $U_{10}$  and  $U \cos(\theta)$  are uncorrelated. A linear regression between these variables shows only a very weak positive correlation ( $R^2 = 0.04$ ), so the use of multiple linear regression to isolate wind speed is reasonable. Equation 10 demonstrates that the variation in  $u_*$  across different current conditions is greater than what is expected from the current-relative wind alone. That is, the observed spread in  $u_*$  (Figure 8) is greater than the prediction shown in Figure 1a. A wave-relative current change of  $0.1 \text{ m s}^{-1}$  was, on average, associated with a change of  $0.0084 \text{ m s}^{-1}$  in  $u_*$  (compared to  $0.0035 \text{ m s}^{-1}$  expected from Equation 2 and Figure 1a). Equation 10 suggests that the range of observed values of wave-relative current of approximately  $0.7 \text{ m s}^{-1}$  will lead to variations in mss and  $u_*$  of 20%, at moderate wind speeds of 8–9  $\text{m s}^{-1}$  (compared to 8% expected from Equation 2 and Figure 1a). However, wave-relative currents did not often vary by this amount at constant wind speeds; the middle 80% of observations within wind bins typically had 0.3–0.35  $\text{m s}^{-1}$  variability in wave-relative currents. Hence, the true typical variation in mss and  $u_*$  is likely around 10%.

Another method of quantifying the influence of surface currents on  $u_*$  is to calculate the difference between the observed  $u_*$  and predicted value from the Large and Pond (1981) relationship, which does not incorporate wave effects, and determine a relationship between this residual  $u_*$  and the wave-relative current. This analysis yielded similar results as the multiple linear regression, with a slightly smaller dependence of wave-relative current on  $u_*$ : residual  $u_*$  decreased by  $0.0057 \text{ ms}^{-1}$  for every  $0.1 \text{ ms}^{-1}$  increase in wave-relative current. These analyses demonstrate that in the ATOMIC study area, which has consistent and strong wave-following currents, small-scale spatial variations in surface currents may drive wave-current interactions and cause significant increases or decreases in  $u_*$  and mss due to wave steepening or flattening, respectively. This is likely also applicable to other regions of the ocean with similar wind speeds and moderate current variability.

These findings support the hypothesis that wave-current interactions in the open ocean significantly modify  $u_*$  when currents strongly follow or oppose the waves. However, the overall variation in observed  $u_*$  is less than the expected spread for a single theoretical wave; that is, there is a greater spread in  $u_*$  at a given wind speed in Figure 1b than in Figure 8. We expect that this discrepancy is primarily due to the directional spread of waves. Calculated from directional moments obtained from SWIFT onboard processing, average wave directional spread in the equilibrium frequency range is around  $45^\circ$ , with typical fluctuations up to  $20^\circ$ . The spread may partially result from scattering effects from submesoscale current velocity variations (Smit & Janssen, 2019), which were commonly observed in this area. The large wave directional spread indicates that a significant portion of the wave spectrum will not be directly aligned with the surface currents when the surface currents oppose or follow the average wave direction. Thus, the net effect of currents on wave steepening or flattening will be lower than expected for a single theoretical wave. The assumption of a constant  $I(p)$  in the calculation of  $u_*$  (Equation 3) may also have contributed to the weaker signal, as directional spreading may covary with the alignment and direction of the waves. In addition, nonlinear interactions and contributions from the lower frequency portion of the spectrum (Vincent et al., 2019) may have smoothed out differences in  $u_*$  between current regimes.

To assess the contribution of wave-current interactions to air-sea momentum flux, we calculate momentum flux from equilibrium  $u_*$  and  $\rho_a$  observations using Equation 1. The physical idea is that mss is a proxy for surface roughness, which is directly related to the wind friction velocity and the momentum flux.  $\rho_a$  was determined from air temperature, air pressure, and relative humidity observations on the v4 SWIFTS. Because relative humidity observations were not available from the v3 SWIFTS, meteorological observations made on the NOAA Ship Ronald H. Brown (Thompson et al., 2021) were used to estimate  $\rho_a$  for these drifters. This approximation had a negligible effect, as  $\rho_a$  varied minimally (mean  $\rho_a$  on the ship was  $1.172 \text{ kg m}^{-3}$  with a standard deviation of  $0.003 \text{ kg m}^{-3}$ ). Momentum flux calculated using  $u_*$  from wave spectra and Equation 1 will hereinafter be referred to as  $\tau_{\text{waves}}$ . We note that using  $\tau_{\text{waves}}$  as a measure of momentum flux is contingent on the assumption that wind-wave equilibrium is valid and spectra follow the theoretical  $f^{-4}$  shape; see Section 4.3 for a discussion. Figure 9a compares wind speed and  $\tau_{\text{waves}}$ :  $\tau_{\text{waves}}$  varies significantly between current conditions for a given wind speed. These differences are statistically significant at moderate wind speeds over  $8 \text{ ms}^{-1}$ . Equation 11,

$$\tau_{\text{waves}} = X + Y U_{10} - Z U \cos(\theta), \quad (11)$$

represents the dependence of  $\tau_{\text{waves}}$  on wind speed and wave-relative current. Performing a multiple linear regression, we find that  $X = -0.116 \pm 0.004$  (standard error),  $Y = 0.028 \pm 0.001$ , and  $Z = -0.061 \pm 0.007$  ( $R^2 = 0.61$ ). As with Equation 10, the short 10-min sampling window likely contributed to uncertainty in these values.  $X$  is an offset and  $Y$  and  $Z$  are the contributions of  $U_{10}$  and  $U \cos(\theta)$  to  $\tau_{\text{waves}}$ .  $\tau_{\text{waves}}$  varies by  $0.0061 \text{ Nm}^{-2}$  on average for a  $0.1 \text{ ms}^{-1}$  change in wave-relative current. This equates to a 40% variation across the entire  $0.7 \text{ ms}^{-1}$  range of observed wave-relative currents at moderate wind speeds of  $8\text{--}9 \text{ ms}^{-1}$  (Equation 11). However, as mentioned above, the true variability at a given wind speed is likely much less than this value, as wave-relative currents typically only varied by a smaller amount. For instance, if wave-relative currents varied by  $0.3 \text{ ms}^{-1}$ ,  $\tau_{\text{waves}}$  would be expected to vary by approximately 17% at  $8\text{--}9 \text{ ms}^{-1}$  winds. This is comparable to the change in momentum flux that would be associated with a wind increase or decrease of  $0.7 \text{ ms}^{-1}$ , according to the Large and Pond (1981) relationship.

Previous studies have shown that wave statistics, including mss, are improved when spectra are normalized by the wave directional spread (Banner et al., 2002; Schwendeman & Thomson, 2015). We recalculated mss from the wave spectra after normalizing spectra by the directional spread ( $\Delta\theta$ ), in addition to the aforementioned normalization by the equilibrium frequency range width: normalizing by  $\Delta\theta$  had a minimal effect on the magnitude

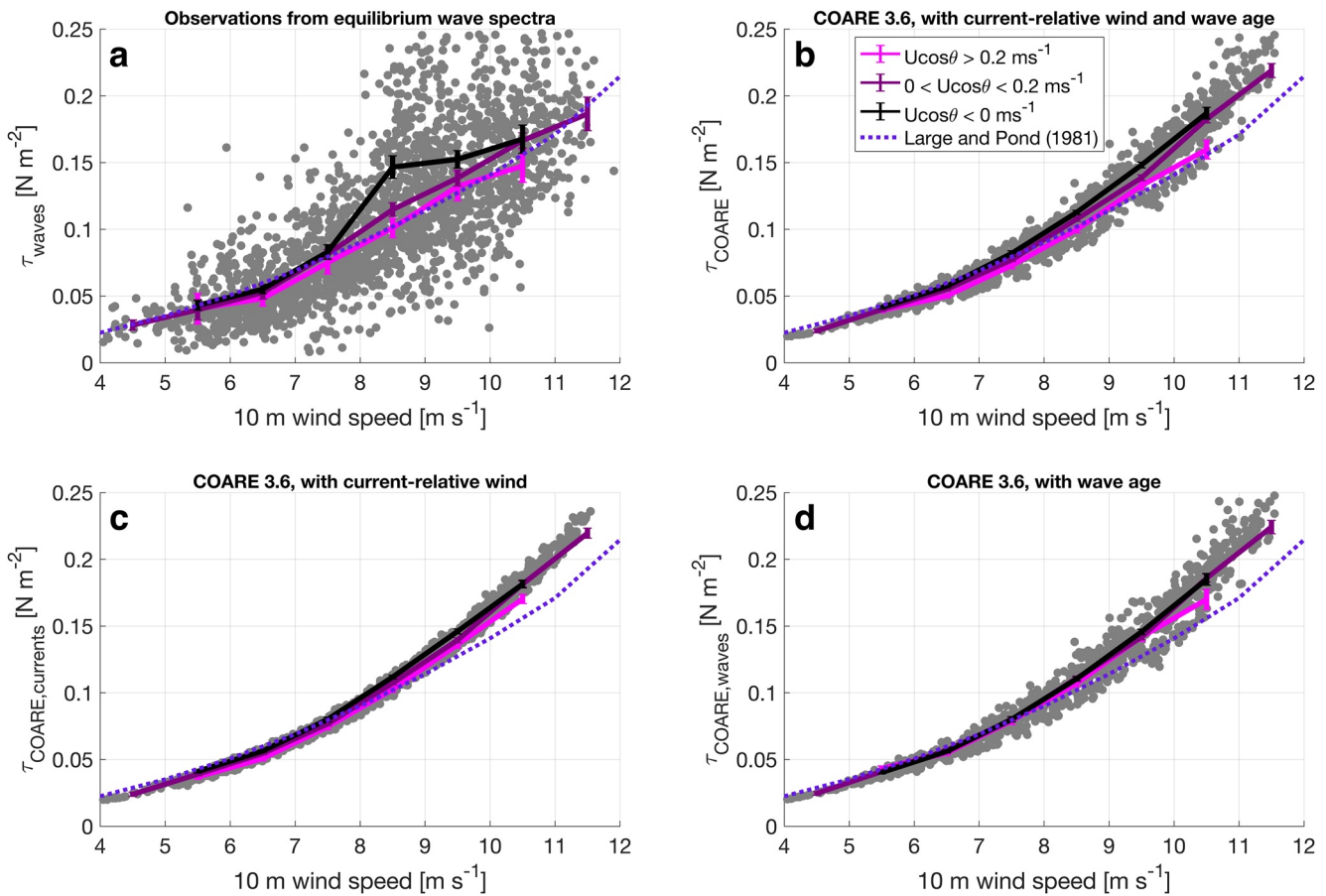


**Figure 9.** Momentum flux versus wind speed calculated from (a) equilibrium  $u_s$  inferred from wave spectra for all Surface Wave Instrument Float with Tracking (SWIFT) data and (b–d) version 3.6 of the COARE algorithm for v4 SWIFT data, during both legs of Atlantic Tradewind Ocean-atmosphere Mesoscale Interaction Campaign. COARE 3.6 inputs included (b) observed surface currents and waves, (c) observed surface currents but not waves, and (d) observed waves but not surface currents. Lines denote averages in  $1 \text{ m s}^{-1}$ -wide wind speed bins, colored by the wave-relative current ( $U \cos \theta$ ). Error bars represent 95% confidence intervals around the mean of each bin. All plotted bins contain a minimum of 10 data points. Gray points represent wind speed and momentum flux observations, smoothed over a 3-hr period. The dotted purple line shows expected values calculated using Equation 1, with  $u_s$  determined by the relationship in Large and Pond (1981) and using the mean  $\rho_a$  observed by the Ronald H. Brown.

of mss; however, it increased the spread in mss between different wave-relative current conditions slightly (not shown). Normalizing by  $\Delta\theta_2$ , the directional spread calculated with the second-order moments of the wave spectra (Thomson et al., 2018), increased the magnitude of mss but did not affect the spread in mss between different current conditions. In short, variance in mss across different wave-relative current conditions exists whether or not spectra are normalized by  $\Delta\theta$  or  $\Delta\theta_2$ . Hence, mss only normalized by the frequency width are shown.

## 4. Discussion and Conclusions

### 4.1. Temporal and Lateral Variations in Surface Currents

The SWIFT observations demonstrate that both temporal and spatial variations in currents exist in the trade wind region encompassing the ATOMIC study area. For instance, case study 1 (Figure 5) shows variations in current speed and direction owing to a combination of increasing or decreasing wind speeds and larger-scale ocean variability, which modified currents throughout the area where drifters were deployed. That is, all drifters observed similar surface current speed and direction at a given time. On the other hand, case study 2 (Figure 6) exhibited spatial variations in surface currents, as winds were relatively steady throughout the domain but current speed and direction varied between drifters that is, drifters at different locations did not observe similar surface currents at the same point in time. This suggests that there is lateral shear in surface currents, which presumably drives



lateral variability in waves and air-sea fluxes. For instance, at 1200 UTC on 15 January 2020 near the beginning of case study 2, the southern two drifters are roughly 30 km apart, with wave-relative currents  $0.17 \text{ ms}^{-1}$  higher (more wave following) at the location of the southernmost drifter (Figure 6).  $u_*$  and  $\tau_{\text{waves}}$  are  $0.060 \text{ ms}^{-1}$  and  $0.043 \text{ Nm}^{-2}$  larger at the location of the southernmost drifter (not shown). This implies that an average lateral wave-relative current shear of just under  $0.006 \text{ ms}^{-1} \text{ km}^{-1}$  is responsible for average lateral variations of  $0.002 \text{ ms}^{-1} \text{ km}^{-1}$  and  $0.0015 \text{ Nm}^{-2}$  in  $u_*$  and  $\tau_{\text{waves}}$ . We note that these shear estimates are highly dependent on the scale of the observations, that is, the spacing between SWIFT drifters. For instance, if a temperature front is sharp, shear will be much stronger in the small region near the front and weaker away from it. This is an important caveat in the context of wave-current interactions: these wave-current interactions only will occur if waves propagate across a region with spatial current variations; otherwise, any change in wave properties is likely due to the current-relative wind alone. Nevertheless, the significant variations observed by drifters across fronts imply that shear is present at some locations between the drifters. This, along with the small-scale features highlighted in Case 1, demonstrates that spatial variations of wave-current interactions are a major source of uncertainty in studies assuming that currents are uniform on submesoscales or mesoscales. That is, surface currents influence mss,  $u_*$ , and momentum flux both when currents are spatially variable and when currents are spatially homogeneous but temporally variable.

#### 4.2. Applications to Air-Sea Interaction and Fluxes

The latest version (3.6) of the widely used Coupled Ocean-Atmosphere Response Experiment (COARE) bulk flux algorithm (Edson et al., 2013; Fairall et al., 2003) utilizes a wave model (Banner & Morison, 2010) to parameterize the effect of wave age on surface roughness and stress through the dominant wave phase speed (i.e., speed at the spectral peak), significant wave height, and wind speed, but does not consider the effects of surface currents on waves other than through changes in the current-relative wind speed (Equation 2). Because the results from Section 3 indicate that wave-current interactions significantly modulate momentum flux when spatial variability exists, we compare COARE 3.6 output, including and excluding parameterizations of the current-relative wind and wave age, to observations to evaluate the significance of wave-current interactions in modulating fluxes and gain insight into the effectiveness of COARE 3.6 parameterizations of momentum flux when surface currents are variable.

Momentum flux calculated using the COARE algorithm ( $\tau_{\text{COARE}}$ ), wind speed, surface current, and wave conditions observed by the SWIFTS and other atmospheric conditions observed at the Ronald H. Brown is shown in Figure 9b. Figure 9c shows momentum flux calculated using COARE 3.6 and prescribing observed surface currents but not waves (i.e., identical to 9b except without wave height and peak period prescribed as an input). Figure 9d shows momentum flux calculated using COARE 3.6 and prescribing observed wave conditions but not surface currents. Wave phase speeds input into COARE were calculated from the observed wave peak period and deep-water wave dispersion relation. Even though centroid period is a more stable parameter that is independent of the frequency spacing of the spectra, we use peak period as the dominant wave period input into COARE because the current version of the COARE algorithm was developed using peak period. v3 and v4 SWIFT peak periods are inconsistent because of the tilting bias discussed earlier, so only v4 SWIFT data were used to calculate momentum flux using COARE.

Figures 9b–9d indicate that the variability of  $\tau_{\text{COARE}}$  at a given wind speed is due to both variations in current-relative wind (Figure 9c) and wave age (Figure 9d). At wind speeds under  $10 \text{ ms}^{-1}$ , there is a larger difference between current conditions when only current-relative wind is prescribed (Figure 9c) than when just wave age is prescribed (Figure 9d). This indicates that the spread in  $\tau_{\text{COARE}}$  between different wave-relative current conditions (Figure 9b) is largely the result of current-relative wind variations rather than waves, although waves do appear to have a significant impact at the highest wind speeds. The variations in  $\tau$  are much larger in the observations (gray points in Figure 9a) than in COARE (gray points in Figures 9b–9d). This results from both variability in waves and turbulence and the inconsistencies in the assumptions used to calculate  $\tau$ . Specifically, variations in the wave spectral slope (Figure 3c), the short 10-min duration over which wave spectra were calculated from, and the assumptions of constant  $\beta$  and  $I(p)$  all contribute uncertainty to  $\tau$  estimates and result in inconsistencies between observed  $\tau$  and COARE estimates or the Large and Pond (1981) parameterization. Furthermore, COARE is designed to represent the mean stress observed under given conditions rather than capture turbulent fluctuations inherent in the real world. However, the variability in bin-averaged  $\tau$  between current conditions estimated

**Table 1**  
Mean Observed and Expected Momentum Flux ( $\tau$ , in  $\text{Nm}^{-2}$ ) Within Wind Speed Bins, as Shown in Figures 9a and 9c

Wind speed	5–6 $\text{ms}^{-1}$	6–7 $\text{ms}^{-1}$	7–8 $\text{ms}^{-1}$	8–9 $\text{ms}^{-1}$	9–10 $\text{ms}^{-1}$	10–11 $\text{ms}^{-1}$
$\tau_{\text{waves}}, U \cos\theta < 0$	0.0431	0.0554	0.0832	0.1469	0.1527	0.1677
$\tau_{\text{waves}}, 0 < U \cos\theta < 0.2$	0.0399	0.0528	0.0815	0.1149	0.1386	0.1667
$\tau_{\text{waves}}, U \cos\theta > 0.2$	0.0406	0.0483	0.0751	0.1012	0.1324	0.1477
$\tau_{\text{COARE}}, U \cos\theta < 0$	0.0410	0.0564	0.0802	0.1117	0.1460	0.1814
$\tau_{\text{COARE}}, 0 < U \cos\theta < 0.2$	0.0391	0.0546	0.0766	0.1073	0.1395	0.1814
$\tau_{\text{COARE}}, U \cos\theta > 0.2$	0.0370	0.0507	0.0745	0.1025	0.1362	0.1703
Current effect in $\tau_{\text{waves}}$	6.0%	13.7%	10.2%	36.8%	14.2%	12.7%
Current effect in $\tau_{\text{COARE}}$	10.3%	10.6%	7.4%	8.6%	7.0%	6.3%

Note. “Current effect” refers to the percent difference between mean values of  $\tau$  in the  $U \cos\theta < 0$  versus  $U \cos\theta > 0.2 \text{ ms}^{-1}$  wave-relative current bins.

using COARE (spread between lines in Figure 9b) is also much smaller than in the observations (spread between lines in Figure 9a). Because random error will be averaged out, we conclude that the smaller spread in COARE estimates is likely not due to the sources of uncertainty mentioned above and instead may be a result of current variability.

Table 1 shows mean  $\tau$  within individual wind speed bins in Figures 9a and 9c. Because Figure 9c does not consider waves, the difference in  $\tau$  between Figures 9a and 9c is an estimate of the influence of waves on momentum flux. At wind speeds above  $8 \text{ ms}^{-1}$ ,  $\tau_{\text{waves}}$  varies by 12.7%–36.8%, while  $\tau_{\text{COARE}}$  only varies by 6.3%–8.6% (Figure 9, Table 1). At these wind speeds, the difference between  $\tau_{\text{waves}}$  and  $\tau_{\text{COARE}}$  within individual bins is at least 6%, suggesting that wave-current interactions may be responsible for variations in  $\tau$  of at least 6%. The variability in  $\tau$  in the  $8\text{--}9 \text{ ms}^{-1}$  wind speed bin suggests significantly greater variability; however, the cause of this is unclear. One possibility is the presence of greater spatial variability in wave-relative currents when winds are moderate.

We note that the wave age parameterization in COARE, which does not incorporate wave-current interactions, reproduces some of the spread between current conditions at wind speeds above  $10 \text{ ms}^{-1}$  (Figures 9b and 9d). This may imply that wave-current interactions are not solely responsible for this variability. However, the spread is not reproduced at slightly lower wind speeds:  $\tau_{\text{COARE}}$  shown in Figures 9b and 9c are typically within a few percent at all wind speeds below  $10 \text{ ms}^{-1}$  (Table 1). At wind speeds below  $8 \text{ ms}^{-1}$ ,  $\tau_{\text{waves}}$  is only associated with a small amount of additional variability compared to  $\tau_{\text{COARE}}$  (Figure 9, Table 1), which suggests that variations in  $\tau$  between different wave-relative current conditions at low wind speeds are primarily the result of current-relative winds rather than wave-current interactions.

Wave-current interactions are expected to have a second-order role in modulating the spatial variations of physical processes in addition to the air-sea momentum flux, including near-surface turbulence, gas transfer, and air-sea sensible, latent, buoyancy, and net heat fluxes. As discussed earlier, steeper wave slopes on one side of a front have previously been observed to be associated with enhanced wave breaking (e.g., Romero et al., 2017; Romero et al., 2020, and others), a process which elevates near-surface turbulent kinetic energy (TKE) dissipation rates (e.g., Agrawal et al., 1992; Craig & Banner, 1994; Terray et al., 1996; Thomson, 2012, and others) and air-sea gas transfer velocities (e.g., Asher et al., 1996; Keeling, 1993; Melville, 1996, and others). Thus, the observed submesoscale spatial variations in mss suggest that air-sea gas exchange and near-surface turbulence vary on the same spatial scales of kilometers to tens of kilometers. Air-sea heat fluxes are influenced by momentum fluxes and would also be expected to vary on the same spatial scales. Assuming standard bulk flux relationships between  $\tau$ , the drag coefficient  $C_D$ , the transfer coefficients of heat and moisture, and the surface heat flux (as shown in Fairall et al., 1996) and assuming that only surface stress is modified and other terms remain the same, a 6% uncertainty in bulk momentum flux will lead to an uncertainty of approximately 3%, or  $6 \text{ Wm}^{-2}$ , of the air-sea sensible plus latent heat flux under average conditions observed during ATOMIC. As mentioned in Section 3.3, a direct comparison between  $\tau_{\text{waves}}$  and direct or parameterized flux estimates (i.e.,  $\tau_{\text{COARE}}$ ) requires assuming that wave spectra used in the calculation of  $\tau_{\text{waves}}$  follow a  $f^{-4}$  shape and wind and waves are in equilibrium. Time- and frequency-averaged spectra had a slope close to  $f^{-4}$  (Figures 3a and 3c), although small deviations from the expected  $f^{-4}$  shape occurred in a considerable number of spectra. Regardless, mss calculated from the spectra

(directly proportional to  $u_*$  used to calculate  $\tau_{\text{waves}}$ , as seen in Equation 5) are indicative of the surface roughness and thus will modulate air-sea momentum fluxes, even if wind-wave equilibrium is not strictly satisfied.

Wind directions are relatively invariant in the ATOMIC study area. Many other areas of the world ocean have similarly consistent wind directions, including the tropics and midlatitudes with prevailing trade winds and westerlies, respectively. Because of this, the observed influence of current variability on waves and momentum flux in the ATOMIC region, as well as the hypothesized influence of current variability on near-surface turbulence, gas exchange, and heat fluxes, is likely applicable to other areas; that is, wave-current interactions may be globally significant in modulating small-scale variability in waves and air-sea interaction even outside of locations with large wind or current variations. This finding is of particular relevance to model simulations that do not account for small-scale spatial variations in surface currents, or those that do not incorporate wave-current interactions at all or comprehensively into air-sea flux parameterizations. Due to greater small-scale spatial variability in coastal areas, the influence of wave-current interactions on air-sea fluxes is likely significantly greater here, along with locations that have stronger mesoscale and submesoscale eddy activity such as near strong western boundary currents like the North Brazil Current region to the south of the ATOMIC study area (Figure 2).

## 5. Conclusions

Typically, in the northwest tropical Atlantic trade wind region during winter, currents follow the waves at  $0\text{--}0.2\text{ ms}^{-1}$ . Conditions where currents were in the opposite direction as the waves occurred approximately 32% of the time, preferentially when wind speeds were below  $8\text{ ms}^{-1}$ . Opposing wave-relative currents were never greater than  $0.24\text{ ms}^{-1}$ . The two case studies demonstrate that surface current speed and directional variability exist on a wide range of spatial scales, from a few kilometers (Figure 5) to the scales of mesoscale features (Figure 6), and produce variations in mss and  $u_*$  on the same scales.

In conditions where the currents follow the waves (green and blue lines in Figure 8), mss and  $u_*$  deviate by 10% from conditions where the currents are neutral or wave opposing (pink and orange lines in Figure 8) in moderate wind conditions. Significant variations in mss and  $u_*$  also are present across different levels of wave-following current conditions. Variability in mss and  $u_*$  is greater than expected from the current-relative wind speed alone (Figure 1a), which implies that variability in  $u_*$  at constant wind speeds is the result of a combination of the current-relative wind and wave-current interactions. The Doppler shift changes the waves' slopes when currents vary spatially, and these changes in roughness are used to infer changes in momentum flux.

These findings suggest that wave-current interactions are a source of uncertainty in predictions of mss or  $u_*$  from either wind speed or current-relative wind speed alone and predictions of wind speed from  $u_*$  such as those by Voermans et al. (2020). Variations in  $u_*$  of 10% roughly equate to variations in momentum flux of 20% at a given wind speed (Equation 1). This significant contribution suggests that the inclusion of current-relative winds and wave-current interactions in models and parameterizations is crucial for obtaining accurate estimates of waves, near-surface turbulence, and air-sea heat, gas, and momentum fluxes. Existing parameterizations of waves and surface currents, such as those from version 3.6 of the COARE bulk flux algorithm, do not comprehensively consider the effect of wave-current interactions. Hence, even though the mean flux is still well represented by these models, they may underestimate variability in air-sea fluxes in the presence of varying surface currents and waves.

## Data Availability Statement

SWIFT data are available through NOAA National Centers for Environmental Information (NCEI) at <https://doi.org/10.25921/s5d7-tc07> (Thomson et al., 2021). Meteorological observations from the NOAA Ship Ronald H. Brown are also available through NOAA NCEI at <https://doi.org/10.25921/etxb-ht19>. Coastline data in Figure 2 were obtained using the NOAA Global Self-consistent Hierarchical High-resolution Geography Database (GSHHG). Reprocessed satellite sea level anomalies used to calculate eddy kinetic energy are available through CMEMS at [https://resources.marine.copernicus.eu/?option=com\\_csw&view=details&product\\_id=SEA-LEVEL\\_GLO\\_PHY\\_L4\\_REP\\_OBSERVATIONS\\_008\\_047](https://resources.marine.copernicus.eu/?option=com_csw&view=details&product_id=SEA-LEVEL_GLO_PHY_L4_REP_OBSERVATIONS_008_047). Version 3.6 of the COARE bulk flux algorithm is available at [ftp://ftp1.esrl.noaa.gov/BLO/Air-Sea/bulkalg/cor3\\_6/](ftp://ftp1.esrl.noaa.gov/BLO/Air-Sea/bulkalg/cor3_6/). Perceptually uniform colormaps used in Figure 2 were obtained from the cmocean package (Thyng et al., 2016).

### Acknowledgments

We thank Kristin Zeiden (APL-UW) for reviewing a version of the manuscript and providing many valuable suggestions. We thank Alex de Klerk (APL-UW) for engineering the SWIFT drifters and for extensive assistance in deploying and recovering the vehicles. We thank Joe Talbert (APL-UW) for engineering the SWIFTS. We appreciate conversations with Chris Fairall (NOAA PSL) regarding the COARE algorithm. We acknowledge the scientists, captain, and crew on the two cruise legs of the 2020 ATOMIC field campaign on the NOAA Ship Ronald H. Brown for their assistance in collecting much of the observational data used in this study. This work was supported by NOAA CPO CVP Award NA19OAR4310374. We thank three anonymous reviewers for numerous comments and suggestions which greatly improved the manuscript.

### References

- Agrawal, Y. C., Terray, E. A., Donelan, M. A., Hwang, P. A., Williams, A. J., III, Drennan, W. M., et al. (1992). Enhanced dissipation of kinetic energy beneath surface waves. *Nature*, 359(6392), 219. <https://doi.org/10.1038/359219a0>
- Akan, Ç., McWilliams, J. C., Moghimi, S., & Özkan-Haller, H. T. (2018). Frontal dynamics at the edge of the Columbia River plume. *Ocean Modelling*, 122, 1–12. <https://doi.org/10.1016/j.ocemod.2017.12.001>
- Akan, Ç., Moghimi, S., Özkan-Haller, H. T., Osborne, J., & Kurapov, A. (2017). On the dynamics of the mouth of the Columbia River: Results from a three-dimensional fully coupled wave-current interaction model. *Journal of Geophysical Research: Oceans*, 122(7), 5218–5236. <https://doi.org/10.1002/2016JC012307>
- Arduin, F., Chapron, B., & Elfouhaily, T. (2004). Waves and the air–sea momentum budget: Implications for ocean circulation modeling. *Journal of Physical Oceanography*, 34(7), 1741–1755. [https://doi.org/10.1175/1520-0485\(2004\)034<1741:watamb>2.0.co;2](https://doi.org/10.1175/1520-0485(2004)034<1741:watamb>2.0.co;2)
- Arduin, F., Gille, S. T., Menemenlis, D., Rocha, C. B., Raschle, N., Chapron, B., et al. (2017). Small-scale open ocean currents have large effects on wind wave heights. *Journal of Geophysical Research: Oceans*, 122(6), 4500–4517. <https://doi.org/10.1002/2016JC012413>
- Asher, W., Karle, L., Higgins, B., Farley, P., Monahan, E., & Leifer, I. (1996). The influence of bubble plumes on air-seawater gas transfer velocities. *Journal of Geophysical Research: Oceans*, 101(C5), 12027–12041. <https://doi.org/10.1029/96JC00121>
- Banihashemi, S., & Kirby, J. T. (2019). Approximation of wave action conservation in vertically sheared mean flows. *Ocean Modelling*, 143, 101460. <https://doi.org/10.1016/j.ocemod.2019.101460>
- Banihashemi, S., Kirby, J. T., & Dong, Z. (2017). Approximation of wave action flux velocity in strongly sheared mean flows. *Ocean Modelling*, 116, 33–47. <https://doi.org/10.1016/j.ocemod.2017.06.002>
- Banner, M. L. (1990). Equilibrium spectra of wind waves. *Journal of Physical Oceanography*, 20(7), 966–984. [https://doi.org/10.1175/1520-0485\(1990\)020<0966:esoww>2.0.co;2](https://doi.org/10.1175/1520-0485(1990)020<0966:esoww>2.0.co;2)
- Banner, M. L., Gemmrich, J. R., & Farmer, D. M. (2002). Multiscale measurements of ocean wave breaking probability. *Journal of Physical Oceanography*, 32(12), 3364–3375. [https://doi.org/10.1175/1520-0485\(2002\)032<3364:mnoowb>2.0.co;2](https://doi.org/10.1175/1520-0485(2002)032<3364:mnoowb>2.0.co;2)
- Banner, M. L., & Morison, R. P. (2010). Refined source terms in wind wave models with explicit wave breaking prediction. Part I: Model framework and validation against field data. *Ocean Modelling*, 33(1–2), 177–189. <https://doi.org/10.1016/j.ocemod.2010.01.002>
- Branch, R. A., Horner-Devine, A. R., Akan, C., Chickadel, C. C., Farquharson, G., Hudson, A., et al. (2018). Airborne LiDAR measurements and model simulations of tides, waves, and surface slope at the mouth of the Columbia River. *IEEE Transactions on Geoscience and Remote Sensing*, 56(12), 7038–7048. <https://doi.org/10.1109/TGRS.2018.2847561>
- Businger, J., & Shaw, W. (1984). The response of the marine boundary layer to mesoscale variations in sea-surface temperature. *Dynamics of Atmospheres and Oceans*, 8(3–4), 267–281. [https://doi.org/10.1016/0377-0265\(84\)90012-5](https://doi.org/10.1016/0377-0265(84)90012-5)
- Campana, J., Terrill, E. J., & De Paolo, T. (2016). The development of an inversion technique to extract vertical current profiles from X-band radar observations. *Journal of Atmospheric and Oceanic Technology*, 33(9), 2015–2028. <https://doi.org/10.1175/JTECH-D-15-0145.1>
- Chawla, A., & Kirby, J. T. (2002). Monochromatic and random wave breaking at blocking points. *Journal of Geophysical Research*, 107(C7), 4–1. <https://doi.org/10.1029/2001JC001042>
- Chelton, D. B., Esbensen, S. K., Schlax, M. G., Thum, N., Freilich, M. H., Wentz, F. J., et al. (2001). Observations of coupling between surface wind stress and sea surface temperature in the eastern tropical Pacific. *Journal of Climate*, 14(7), 1479–1498. [https://doi.org/10.1175/1520-0442\(2001\)014<1479:oochsw>2.0.co;2](https://doi.org/10.1175/1520-0442(2001)014<1479:oochsw>2.0.co;2)
- Chelton, D. B., Schlax, M. G., Freilich, M. H., & Milliff, R. F. (2004). Satellite measurements reveal persistent small-scale features in ocean winds. *Science*, 303(5660), 978–983. <https://doi.org/10.1126/science.1091901>
- Chen, H., & Zou, Q. (2018). Characteristics of wave breaking and blocking by spatially varying opposing currents. *Journal of Geophysical Research: Oceans*, 123(5), 3761–3785. <https://doi.org/10.1029/2017JC013440>
- Choi, W. (2009). Nonlinear surface waves interacting with a linear shear current. *Mathematics and Computers in Simulation*, 80(1), 29–36. <https://doi.org/10.1016/j.matcom.2009.06.021>
- Coles, V. J., Brooks, M. T., Hopkins, J., Stukel, M. R., Yager, P. L., & Hood, R. R. (2013). The pathways and properties of the Amazon river plume in the tropical north Atlantic ocean. *Journal of Geophysical Research: Oceans*, 118(12), 6894–6913. <https://doi.org/10.1002/2013JC008981>
- Collins, C., Potter, H., Lund, B., Tamura, H., & Graber, H. C. (2018). Directional wave spectra observed during intense tropical cyclones. *Journal of Geophysical Research: Oceans*, 123(2), 773–793. <https://doi.org/10.1002/2017JC012943>
- Craig, P. D., & Banner, M. L. (1994). Modeling wave-enhanced turbulence in the ocean surface layer. *Journal of Physical Oceanography*, 24(12), 2546–2559. [https://doi.org/10.1175/1520-0485\(1994\)024<2546:mwetit>2.0.co;2](https://doi.org/10.1175/1520-0485(1994)024<2546:mwetit>2.0.co;2)
- Ebuchi, N., & Hanawa, K. (2000). Mesoscale eddies observed by TOLEX-ADCP and TOPEX/POSEIDON altimeter in the Kuroshio recirculation region south of Japan. *Journal of Oceanography*, 56(1), 43–57. <https://doi.org/10.1023/A:1011110507628>
- Edson, J. B., Jampana, V., Weller, R. A., Bigorre, S. P., Plueddemann, A. J., Fairall, C. W., et al. (2013). On the exchange of momentum over the open ocean. *Journal of Physical Oceanography*, 43(8), 1589–1610. <https://doi.org/10.1175/JPO-D-12-0173.1>
- Ellingsen, S. Å., & Li, Y. (2017). Approximate dispersion relations for waves on arbitrary shear flows. *Journal of Geophysical Research: Oceans*, 122(12), 9889–9905. <https://doi.org/10.1002/2017JC012994>
- Fairall, C. W., Bradley, E. F., Hare, J., Grachev, A. A., & Edson, J. B. (2003). Bulk parameterization of air–sea fluxes: Updates and verification for the COARE algorithm. *Journal of Climate*, 16(4), 571–591. [https://doi.org/10.1175/1520-0442\(2003\)016<0571:bpoasf>2.0.co;2](https://doi.org/10.1175/1520-0442(2003)016<0571:bpoasf>2.0.co;2)
- Fairall, C. W., Bradley, E. F., Rogers, D. P., Edson, J. B., & Young, G. S. (1996). Bulk parameterization of Air-sea fluxes for tropical ocean-global atmosphere coupled-ocean atmosphere response experiment. *Journal of Geophysical Research: Oceans*, 101(C2), 3747–3764. <https://doi.org/10.1029/95JC03205>
- Pfiedel, A. (2005). North Brazil current rings viewed by TRMM microwave imager SST and the influence of the Amazon plume. *Deep Sea Research Part I: Oceanographic Research Papers*, 52(1), 137–160. <https://doi.org/10.1016/j.dsr.2004.05.013>
- Fisher, A. W., Sanford, L. P., Scully, M. E., & Suttles, S. E. (2017). Surface wave effects on the translation of wind stress across the air–sea interface in a fetch-limited, coastal embayment. *Journal of Physical Oceanography*, 47(8), 1921–1939. <https://doi.org/10.1175/JPO-D-16-0146.1>
- Fratantoni, D. M., & Glickson, D. A. (2002). North Brazil Current ring generation and evolution observed with SeaWiFS. *Journal of Physical Oceanography*, 32(3), 1058–1074. [https://doi.org/10.1175/1520-0485\(2002\)032<1058:nbcrga>2.0.co;2](https://doi.org/10.1175/1520-0485(2002)032<1058:nbcrga>2.0.co;2)
- Fratantoni, D. M., & Richardson, P. L. (2006). The evolution and demise of North Brazil Current rings. *Journal of Physical Oceanography*, 36(7), 1241–1264. <https://doi.org/10.1175/JPO2907.1>
- Friehe, C., Shaw, W., Rogers, D., Davidson, K., Large, W., Stage, S., et al. (1991). Air-sea fluxes and surface layer turbulence around a sea surface temperature front. *Journal of Geophysical Research*, 96(C5), 8593–8609. <https://doi.org/10.1029/90JC02062>
- Gaube, P., Chelton, D. B., Samelson, R. M., Schlax, M. G., & O’Neill, L. W. (2015). Satellite observations of mesoscale eddy-induced Ekman pumping. *Journal of Physical Oceanography*, 45(1), 104–132. <https://doi.org/10.1175/JPO-D-14-0032.1>



- Gemrich, J., & Garrett, C. (2012). The signature of inertial and tidal currents in offshore wave records. *Journal of Physical Oceanography*, 42(6), 1051–1056. <https://doi.org/10.1175/JPO-D-12-043.1>
- Gemrich, J., & Pawlowicz, R. (2020). Wind waves in the strait of Georgia. *Atmosphere-Ocean*, 58(2), 79–97. <https://doi.org/10.1080/07055900.2020.1735989>
- Haus, B. K. (2007). Surface current effects on the fetch-limited growth of wave energy. *Journal of Geophysical Research*, 112(C3). <https://doi.org/10.1029/2006JC003924>
- Hegermiller, C. A., Warner, J. C., Olabarrieta, M., & Sherwood, C. R. (2019). Wave-current interaction between hurricane Matthew wave fields and the Gulf stream. *Journal of Physical Oceanography*, 49(11), 2883–2900. <https://doi.org/10.1175/JPO-D-19-0124.1>
- Herrera, J., González, J., & Varela, R. (2019). Measuring a Lagrangian drifter's slip with an onboard adcp. *MethodsX*, 6, 1336–1342. <https://doi.org/10.1016/j.mex.2019.05.032>
- Holthuijsen, L., & Tolman, H. (1991). Effects of the Gulf stream on ocean waves. *Journal of Geophysical Research*, 96(C7), 12755–12771. <https://doi.org/10.1029/91JC00901>
- Janssen, P. A. (1989). Wave-induced stress and the drag of air flow over sea waves. *Journal of Physical Oceanography*, 19(2), 745–754. [https://doi.org/10.1175/1520-0485\(1989\)019<0745:wisatd>2.0.co;2](https://doi.org/10.1175/1520-0485(1989)019<0745:wisatd>2.0.co;2)
- Juszko, B.-A., Marsden, R. F., & Waddell, S. R. (1995). Wind stress from wave slopes using Phillips equilibrium theory. *Journal of Physical Oceanography*, 25(2), 185–203. [https://doi.org/10.1175/1520-0485\(1995\)025<0185:wswfsu>2.0.co;2](https://doi.org/10.1175/1520-0485(1995)025<0185:wswfsu>2.0.co;2)
- Kastner, S. E., Horner-Devine, A. R., & Thomson, J. (2018). The influence of wind and waves on spreading and mixing in the Fraser River plume. *Journal of Geophysical Research: Oceans*, 123(9), 6818–6840. <https://doi.org/10.1029/2018JC013765>
- Keeling, R. F. (1993). On the role of large bubbles in air-sea gas exchange and supersaturation in the ocean. *Journal of Marine Research*, 51(2), 237–271. <https://doi.org/10.1357/0022240933223800>
- Kim, S. Y. (2010). Observations of submesoscale eddies using high-frequency radar-derived kinematic and dynamic quantities. *Continental Shelf Research*, 30(15), 1639–1655. <https://doi.org/10.1016/j.csr.2010.06.011>
- Kirby, J. T., & Chen, T.-M. (1989). Surface waves on vertically sheared flows: Approximate dispersion relations. *Journal of Geophysical Research*, 94(C1), 1013–1027. <https://doi.org/10.1029/JC094iC01p01013>
- Kitaigorodskii, S. (1983). On the theory of the equilibrium range in the spectrum of wind-generated gravity waves. *Journal of Physical Oceanography*, 13(5), 816–827. [https://doi.org/10.1175/1520-0485\(1983\)013<0816:ottote>2.0.co;2](https://doi.org/10.1175/1520-0485(1983)013<0816:ottote>2.0.co;2)
- Kudryavtsev, V., Yurovskaya, M., Chapron, B., Collard, F., & Donlon, C. (2017). Sun glitter imagery of surface waves. part 2: Waves transformation on ocean currents. *Journal of Geophysical Research: Oceans*, 122(2), 1384–1399. <https://doi.org/10.1002/2016JC012426>
- Large, W., & Pond, S. (1981). Open ocean momentum flux measurements in moderate to strong winds. *Journal of Physical Oceanography*, 11(2), 324–336. [https://doi.org/10.1175/1520-0485\(1981\)011<0324:oofmi>2.0.co;2](https://doi.org/10.1175/1520-0485(1981)011<0324:oofmi>2.0.co;2)
- Laxague, N. J., Özgökmen, T. M., Haus, B. K., Novelli, G., Shcherbina, A., Sutherland, P., et al. (2018). Observations of near-surface current shear help describe oceanic oil and plastic transport. *Geophysical Research Letters*, 45(1), 245–249. <https://doi.org/10.1002/2017GL075891>
- Lenain, L., & Melville, W. K. (2017). Measurements of the directional spectrum across the equilibrium saturation ranges of wind-generated surface waves. *Journal of Physical Oceanography*, 47(8), 2123–2138. <https://doi.org/10.1175/JPO-D-17-0017.1>
- Lindzen, R. S., & Nigam, S. (1987). On the role of sea surface temperature gradients in forcing low-level winds and convergence in the tropics. *Journal of the Atmospheric Sciences*, 44(17), 2418–2436. [https://doi.org/10.1175/1520-0469\(1987\)044<2418:otross>2.0.co;2](https://doi.org/10.1175/1520-0469(1987)044<2418:otross>2.0.co;2)
- Lygre, A., & Krogstad, H. E. (1986). Maximum entropy estimation of the directional distribution in ocean wave spectra. *Journal of Physical Oceanography*, 16(12), 2052–2060. [https://doi.org/10.1175/1520-0485\(1986\)016<2052:mecotd>2.0.co;2](https://doi.org/10.1175/1520-0485(1986)016<2052:mecotd>2.0.co;2)
- McWilliams, J. C. (2016). Submesoscale currents in the ocean. *Proceedings of the Royal Society A: Mathematical, Physical & Engineering Sciences*, 472(2189), 20160117. <https://doi.org/10.1098/rspa.2016.0117>
- McWilliams, J. C. (2018). Surface wave effects on submesoscale fronts and filaments. *Journal of Fluid Mechanics*, 843, 479. <https://doi.org/10.1017/jfm.2018.158>
- Melville, W. K. (1996). The role of surface-wave breaking in air-sea interaction. *Annual Review of Fluid Mechanics*, 28(1), 279–321. <https://doi.org/10.1146/annurev.fl.28.010196.001431>
- Moghimi, S., Özkan-Haller, H. T., Akan, Ç., & Jurisa, J. T. (2019). Mechanistic analysis of the wave-current interaction in the plume region of a partially mixed tidal inlet. *Ocean Modelling*, 134, 110–126. <https://doi.org/10.1016/j.oceomod.2018.12.003>
- Molinari, R. L., Spillane, M., Brooks, I., Atwood, D., & Duckett, C. (1981). Surface currents in the Caribbean Sea as deduced from Lagrangian observations. *Journal of Geophysical Research: Oceans*, 86(C7), 6537–6542. <https://doi.org/10.1029/JC086iC07p06537>
- Niiler, P. P., & Paduan, J. D. (1995). Wind-driven motions in the northeast Pacific as measured by Lagrangian drifters. *Journal of Physical Oceanography*, 25(11), 2819–2830. [https://doi.org/10.1175/1520-0485\(1995\)025<2819:wdmtn>2.0.co;2](https://doi.org/10.1175/1520-0485(1995)025<2819:wdmtn>2.0.co;2)
- Phillips, O. (1984). On the response of short ocean wave components at a fixed wavenumber to ocean current variations. *Journal of Physical Oceanography*, 14(9), 1425–1433. [https://doi.org/10.1175/1520-0485\(1984\)014<1425:otroso>2.0.co;2](https://doi.org/10.1175/1520-0485(1984)014<1425:otroso>2.0.co;2)
- Phillips, O. (1985). Spectral and statistical properties of the equilibrium range in wind-generated gravity waves. *Journal of Fluid Mechanics*, 156, 505–531. <https://doi.org/10.1017/S0022112085002221>
- Pincus, R., Fairall, C. W., Bailey, A., Chen, H., Chuang, P. Y., de Boer, G., et al. (2021). Observations from the NOAA P-3 aircraft during ATOMIC. *Earth System Science Data*, 13(7), 3281–3296. <https://doi.org/10.5194/essd-13-3281-2021>
- Plant, W. J. (1982). A relationship between wind stress and wave slope. *Journal of Geophysical Research*, 87(C3), 1961–1967. <https://doi.org/10.1029/JC087iC03p01961>
- Portilla, J., Ocampo-Torres, F. J., & Monbaliu, J. (2009). Spectral partitioning and identification of wind sea and swell. *Journal of Atmospheric and Oceanic Technology*, 26(1), 107–122. <https://doi.org/10.1175/2008JTECH0609.1>
- Poulain, P.-M., Bussani, A., Gerin, R., Jungwirth, R., Mauri, E., Menna, M., & Notarstefano, G. (2013). Mediterranean surface currents measured with drifters: From basin to subinertial scales. *Oceanography*, 26(1), 38–47. <https://doi.org/10.5670/oceanog.2013.03>
- Quilfen, Y., & Chapron, B. (2019). Ocean surface wave-current signatures from satellite altimeter measurements. *Geophysical Research Letters*, 46(1), 253–261. <https://doi.org/10.1029/2018GL081029>
- Quilfen, Y., Yurovskaya, M., Chapron, B., & Ardhuin, F. (2018). Storm waves focusing and steepening in the Agulhas current: Satellite observations and modeling. *Remote Sensing of Environment*, 216, 561–571. <https://doi.org/10.1016/j.rse.2018.07.020>
- Quinn, P. K., Thompson, E. J., Coffman, D. J., Baidar, S., Bariteau, L., Bates, T. S., et al. (2021). Measurements from the RV Ronald H. Brown and related platforms as part of the Atlantic Tradewind Ocean-atmosphere mesoscale interaction campaign (ATOMIC). *Earth System Science Data*, 13(4), 1759–1790. <https://doi.org/10.5194/essd-13-1759-2021>
- Rapizo, H., Durrant, T. H., & Babanin, A. V. (2018). An assessment of the impact of surface currents on wave modeling in the Southern Ocean. *Ocean Dynamics*, 68(8), 939–955. <https://doi.org/10.1007/s10236-018-1171-7>

- Raschle, N., Chapron, B., Ponte, A., Arduin, F., & Klein, P. (2014). Surface roughness imaging of currents shows divergence and strain in the wind direction. *Journal of Physical Oceanography*, 44(8), 2153–2163. <https://doi.org/10.1175/JPO-D-13-0278.1>
- Raschle, N., Molemaker, J., Marié, L., Nouguier, F., Chapron, B., Lund, B., & Mouche, A. (2017). Intense deformation field at oceanic front inferred from directional sea surface roughness observations. *Geophysical Research Letters*, 44(11), 5599–5608. <https://doi.org/10.1002/2017GL073473>
- Redelsperger, J.-L., Bouin, M.-N., Pianezze, J., Garnier, V., & Marié, L. (2019). Impact of a sharp, small-scale SST front on the marine atmospheric boundary layer on the Iroise Sea: Analysis from a hectometric simulation. *Quarterly Journal of the Royal Meteorological Society*, 145(725), 3692–3714. <https://doi.org/10.1002/qj.3650>
- Reverdin, G., Olivier, L., Foltz, G., Speich, S., Karstensen, J., Horstmann, J., et al. (2021). Formation and evolution of a freshwater plume in the northwestern tropical Atlantic in February 2020. *Journal of Geophysical Research: Oceans*, 126(4), e2020JC016981. <https://doi.org/10.1029/2020JC016981>
- Romero, L., Hypolite, D., & McWilliams, J. C. (2020). Submesoscale current effects on surface waves. *Ocean Modelling*, 153, 101662. <https://doi.org/10.1016/j.ocemod.2020.101662>
- Romero, L., Hypolite, D., & McWilliams, J. C. (2021). Representing wave effects on currents. *Ocean Modelling*, 101873. <https://doi.org/10.1016/j.ocemod.2021.101873>
- Romero, L., Lenain, L., & Melville, W. K. (2017). Observations of surface wave–current interaction. *Journal of Physical Oceanography*, 47(3), 615–632. <https://doi.org/10.1175/JPO-D-16-0108.1>
- Schwendeman, M., & Thomson, J. (2015). Observations of whitecap coverage and the relation to wind stress, wave slope, and turbulent dissipation. *Journal of Geophysical Research: Oceans*, 120(12), 8346–8363. <https://doi.org/10.1002/2015JC011196>
- Shao, M., Ortiz-Suslow, D. G., Haus, B. K., Lund, B., Williams, N. J., Özgökmen, T. M., et al. (2019). The variability of winds and fluxes observed near submesoscale fronts. *Journal of Geophysical Research: Oceans*, 124(11), 7756–7780. <https://doi.org/10.1029/2019JC015236>
- Smit, P. B., & Janssen, T. T. (2019). Swell propagation through submesoscale turbulence. *Journal of Physical Oceanography*, 49(10), 2615–2630. <https://doi.org/10.1175/JPO-D-18-0250.1>
- Smith, S. D. (1980). Wind stress and heat flux over the ocean in gale force winds. *Journal of Physical Oceanography*, 10(5), 709–726. [https://doi.org/10.1175/1520-0485\(1980\)010<0709:wsahfo>2.0.co;2](https://doi.org/10.1175/1520-0485(1980)010<0709:wsahfo>2.0.co;2)
- Stevens, B., Bony, S., Farrell, D., Ament, F., Blyth, A., Fairall, C., et al. (2021). EUREC4A. *Earth System Science Data Discussions*, 1–78. <https://doi.org/10.5194/essd-2021-18>
- Suzuki, N., Fox-Kemper, B., Hamlington, P. E., & Van Roekel, L. P. (2016). Surface waves affect frontogenesis. *Journal of Geophysical Research: Oceans*, 121(5), 3597–3624. <https://doi.org/10.1002/2015JC011563>
- Tang, C., Perrie, W., Jenkins, A., DeTracey, B., Hu, Y., Toulany, B., & Smith, P. (2007). Observation and modeling of surface currents on the grand banks: A study of the wave effects on surface currents. *Journal of Geophysical Research: Oceans*, 112(C10). <https://doi.org/10.1029/2006JC004028>
- Terray, E. A., Donelan, M., Agrawal, Y., Drennan, W. M., Kahma, K., Williams, A. J., et al. (1996). Estimates of kinetic energy dissipation under breaking waves. *Journal of Physical Oceanography*, 26(5), 792–807. [https://doi.org/10.1175/1520-0485\(1996\)026<0792:eokedu>2.0.co;2](https://doi.org/10.1175/1520-0485(1996)026<0792:eokedu>2.0.co;2)
- Thompson, E., Fairall, C., Pezoa, S., & Bariteau, L. (2021). *ATOMIC ship navigation, meteorology, seawater, fluxes: Near-surface meteorology, air-sea fluxes, surface ocean waves, and near surface ocean parameters (temperature, salinity, currents) and primary dataset of ship location and navigation estimated from in-situ and remote sensing instruments aboard NOAA Ship Ronald H. Brown in the north Atlantic ocean, near Barbados: Atlantic Tradewind Ocean-atmosphere mesoscale interaction campaign 2020-01-09 to 2020-02-12 (NCEI accession 0225427)*. NOAA National Centers for Environmental Information. Dataset. <https://doi.org/10.25921/etxb-ht19>
- Thomson, J. (2012). Wave breaking dissipation observed with “SWIFT” drifters. *Journal of Atmospheric and Oceanic Technology*, 29(12), 1866–1882. <https://doi.org/10.1175/JTECH-D-12-00018.1>
- Thomson, J., D’Asaro, E., Cronin, M., Rogers, W., Harcourt, R., & Shcherbina, A. (2013). Waves and the equilibrium range at ocean weather station p. *Journal of Geophysical Research: Oceans*, 118(11), 5951–5962. <https://doi.org/10.1002/2013JC008837>
- Thomson, J., Girton, J. B., Jha, R., & Trapani, A. (2018). Measurements of directional wave spectra and wind stress from a wave glider autonomous surface vehicle. *Journal of Atmospheric and Oceanic Technology*, 35(2), 347–363. <https://doi.org/10.1175/JTECH-D-17-0091.1>
- Thomson, J., Horner-Devine, A. R., Zippel, S., Rusch, C., & Geyer, W. (2014). Wave breaking turbulence at the offshore front of the Columbia River plume. *Geophysical Research Letters*, 41(24), 8987–8993. <https://doi.org/10.1002/2014GL062274>
- Thomson, J., Moulton, M., de Klerk, A., Talbert, J., Guerra, M., Kastner, S., et al. (2019). A new version of the SWIFT platform for waves, currents, and turbulence in the ocean surface layer. In *2019 IEEE/OES Twelfth Current, Waves and Turbulence Measurement (CWTM)*, 1–7. <https://doi.org/10.1109/CWTM43797.2019.8955299>
- Thomson, J., Thomson, E., Iyer, S., Drushka, K., & de Klerk, A. (2021). *ATOMIC SWIFT drifters: Near-surface meteorology, air-sea fluxes, surface ocean waves, and near-surface ocean properties (turbulent dissipation rate, currents, temperature, salinity) estimated from in-situ and remote sensing instruments aboard six SWIFT drifters (Surface Wave Instrument Float with Tracking) launched and recovered for two different deployments from NOAA Ship Ronald H. Brown in the North Atlantic Ocean. Atlantic Tradewind Ocean-atmosphere mesoscale interaction campaign 2020-01-14 to 2020-02-11 (NCEI accession 0225279)*. NOAA National Centers for Environmental Information. Dataset. <https://doi.org/10.25921/s5d7-tc07>
- Thyng, K. M., Greene, C. A., Hetland, R. D., Zimmerle, H. M., & DiMarco, S. F. (2016). True colors of oceanography: Guidelines for effective and accurate colormap selection. *Oceanography*, 29(3), 9–13. <https://doi.org/10.5670/oceanog.2016.66>
- van Aken, H. M. (2002). Surface currents in the Bay of Biscay as observed with drifters between 1995 and 1999. *Deep Sea Research Part I: Oceanographic Research Papers*, 49(6), 1071–1086. [https://doi.org/10.1016/S0967-0637\(02\)00017-1](https://doi.org/10.1016/S0967-0637(02)00017-1)
- van der Westhuisen, A. J. (2012). Spectral modeling of wave dissipation on negative current gradients. *Coastal Engineering*, 68, 17–30. <https://doi.org/10.1016/j.coastaleng.2012.05.001>
- Vincent, C. L., Thomson, J., Graber, H. C., & Collins, C. O., III. (2019). Impact of swell on the wind-sea and resulting modulation of stress. *Progress in Oceanography*, 178, 102164. <https://doi.org/10.1016/j.pocan.2019.102164>
- Voermans, J., Smit, P., Janssen, T., & Babanin, A. (2020). Estimating wind speed and direction using wave spectra. *Journal of Geophysical Research: Oceans*, 125(2), e2019JC015717. <https://doi.org/10.1029/2019JC015717>
- Wallace, J. M., Mitchell, T., & Deser, C. (1989). The influence of sea-surface temperature on surface wind in the eastern equatorial Pacific: Seasonal and interannual variability. *Journal of Climate*, 22(12), 1492–1499. [https://doi.org/10.1175/1520-0442\(1989\)002<1492:tiosst>2.0.co;2](https://doi.org/10.1175/1520-0442(1989)002<1492:tiosst>2.0.co;2)
- Wang, P., & Sheng, J. (2016). A comparative study of wave-current interactions over the eastern Canadian shelf under severe weather conditions using a coupled wave-circulation model. *Journal of Geophysical Research: Oceans*, 121(7), 5252–5281. <https://doi.org/10.1002/2016JC011758>
- Zippel, S., & Thomson, J. (2017). Surface wave breaking over sheared currents: Observations from the mouth of the Columbia river. *Journal of Geophysical Research: Oceans*, 122(4), 3311–3328. <https://doi.org/10.1002/2016JC012498>